NASA TECHNICAL NOTE

NASA TN D-2342

LOAN COPY: RE
AFWL (WL
KIRTLAND AFB

TECH LIBRARY KAFB, NM
0154989

NASA TN D-2342

A PARAMETRIC STUDY OF HYPERSONIC FLOW FIELDS ABOUT BLUNT-NOSED CYLINDERS AT ZERO ANGLE OF ATTACK

by James E. Terry and Carlton S. James

Ames Research Center
Moffett Field, Calif.

NATIONAL AERONAUTICS AND SPACE ADMINISTRATION • WASHINGTON, D. C. • JULY 1964

TECH LIBRARY KAFB, NM

0154989

A PARAMETRIC STUDY OF HYPERSONIC FLOW FIELDS ABOUT BLUNT-NOSED CYLINDERS AT ZERO ANGLE OF ATTACK

By James E. Terry and Carlton S. James

Ames Research Center
Moffett Field, Calif.

NATIONAL AERONAUTICS AND SPACE ADMINISTRATION

For sale by the Office of Technical Services, Department of Commerce,
Washington, D.C. 20230 -- Price $1.50

A PARAMETRIC STUDY OF HYPERSONIC FLOW FIELDS ABOUT BLUNT-NOSED CYLINDERS AT ZERO ANGLE OF ATTACK

By James E. Terry and Carlton S. James

Ames Research Center
Moffett Field, Calif.

SUMMARY

A systematic study has been made of the effects of changes in Mach number, altitude, nose-drag coefficient, and nose shape on the flow fields over the afterbodies of blunt-nosed cylinders traveling at hypersonic speeds. Shock-wave profiles for 3 families of nose shapes were measured at Mach numbers of 5, 10, and 15 and at various stream densities. The flow fields behind these shocks were obtained by stream-tube calculations. It was shown that the shock-wave shape and hence the surface-pressure distribution could not be predicted quantitatively by the blast-wave theory. The rate of decay of surface pressure with x/d was different in equilibrium air from that in a perfect gas. Surface-pressure ratios and shock-wave shape were insensitive to changes in altitude. Temperature, density, and, to a lesser extent, dynamic-pressure ratios vary appreciably with altitude. The thickness of the high-entropy layer near the body increases with both Mach number and drag coefficient. At high drag coefficients, the entropy distribution was relatively insensitive to nose shape. However, at low drag coefficients, the entropy for conical bodies was low near the body compared to that for bodies with detached shock waves, and corresponding differences were found for the temperature, density, and dynamic-pressure ratios near the body. Surface temperature, density, and dynamic-pressure ratios could not be correlated but could be readily computed by means of the surface-pressure correlation data and the entropy behind the appropriate shock wave.

INTRODUCTION

The designer of a vehicle for flight at hypersonic speeds must be able to make a reasonable prediction of the flow field around the body. Several methods have been developed for computing axisymmetric flow fields over blunt bodies which couple method-of-characteristics solutions for the supersonic part of the flow field to a numerical solution of the fluid dynamics equations for the subsonic region (refs. 1-3). These methods are not applicable to bodies with subsonic corners and, in general, are difficult to apply. Seiff and Whiting (ref. 4) proposed a simplified computing method, applicable to the afterbody only, which utilized an assumed form for the pressure distribution between the body and the shock wave, a known shock-wave profile and continuity relations to obtain a solution at any station in the flow field without solving the entire field. A complementary study of shock-wave profiles was presented in reference 5. It is the purpose of this report to present the

results of a systematic study, using the method of reference 4, of the effects of variations in Mach number, nose-drag coefficient, and nose shape on the flow fields over the afterbodies of some sharp and blunt-nosed cylinders. The effects of changes in gas properties (perfect and real gases) are also explored.

Since a prerequisite to the use of the method of reference 4 is the possession of shock-wave profiles, the first part of the present paper is devoted to an experimental program conducted to obtain the required data. The shock-wave profiles were measured from shadowgraphs of gun-launched free-flight models for the following range of parameters: Mach number, 5 to 20; nose-drag coefficient, 0.5 to 1.8; and nose shape, ellipsoids, cones, and sphere-cones. To supplement the single comparison in reference 4 between an "exact" theory and the method of reference 4, these results are then used to generate solutions which can be compared with method-of-characteristics solutions and with experimental pressure distribution results. After the correlation of these various results has been demonstrated, the method of reference 4 is then used to extend the parametric analysis to bodies and flight conditions for which no solutions have heretofore existed.

SYMBOLS

a constant in shock-wave profile equation, defined by equation (3)

C_D nose-drag coefficient as calculated by modified Newtonian theory, ($C_{p_{max}} = 1.8$)

C_p pressure coefficient, $\frac{p - p_\infty}{q_\infty}$

d body diameter

H altitude

k constant in shock-wave equation, defined by equation (3)

M Mach number

M_R Mach number of radial growth of shock wave, $M_R = M_\infty \tan \varphi = M_\infty \frac{dR}{dx}$

n constant in shock-wave equation, defined by equation (3)

p pressure

q dynamic pressure, $\frac{1}{2} \rho V^2$

r model nose radius

R radial coordinate or gas constant

$\overline{R}$ dimensionless distance between body and shock wave, $\frac{R - (R)_{body}}{(R)_{shock} - (R)_{body}}$

Re Reynolds number, $\frac{\rho_\infty V_\infty d}{\mu_\infty}$

s entropy

T temperature

V velocity

x axial coordinate measured from apex of shock wave

γ isentropic exponent, $\left(\frac{\partial \ln p}{\partial \ln \rho}\right)_{\text{constant entropy}} = \left(\frac{C_p}{C_v} \text{ at low temperatures}\right)$

θ surface inclination measured from free-stream velocity vector

μ viscosity

ρ density

φ shock-wave angle, $\tan^{-1} \frac{dR}{dx}$

Subscripts

∞ free-stream value

s behind shock wave

SHOCK-WAVE PROFILES

Experimental Wave Shapes

The experimental program produced shock-wave profiles for systematically varying Mach number, nose-drag coefficient, and nose shape. The models were designed to have drag coefficients of 0.5, 0.9, 1.3, and 1.8 in each of three families of nose shapes: ellipsoids, cones, and sphere-cones (figs. 1 and 2). Drag coefficients were calculated from modified Newtonian pressure distributions ($C_p = 1.8 \sin^2 \theta$) except for the shallow angle cone for which the solutions of reference 6 were used. The models were fired from a light-gas gun in the Ames Supersonic Free-Flight Wind Tunnel at nominal Mach numbers of 5, 10, and 15. Test conditions are tabulated in table I.

The required shock-wave profiles were measured from shadowgraph pictures taken of the models in flight. Sample shadowgraphs are shown in figure 3. A more detailed discussion of the data reduction procedure is given in appendix A. The coordinate system used in this report (sketch (a)) differs from that used in many reports in that the origin is at the apex of the shock wave rather than the apex of the model.

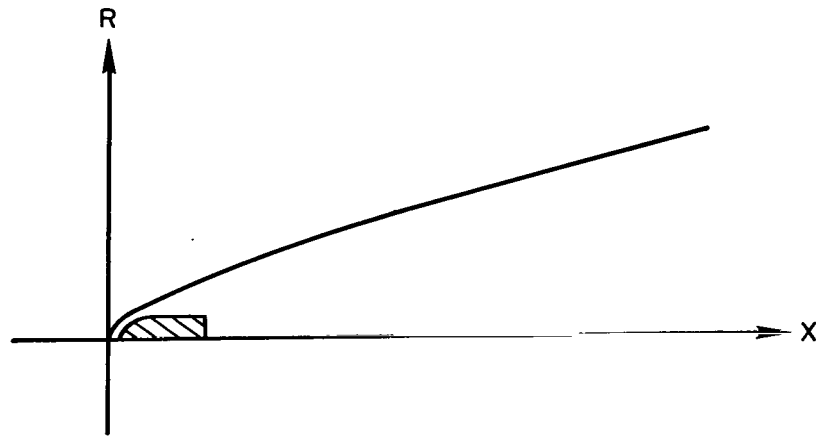

Sketch (a)

The effects of the three test variables on shock-wave shape are displayed most clearly when the wave profiles are plotted in logarithmic coordinates; see figures 4 and 5. The profiles of figure 4 are arranged to show the dependence on Mach number and drag coefficient for the ellipsoid family. Figure 5 illustrates the combined effects of nose shape and drag coefficient. It is apparent that some portions of the shock-wave profiles are exponential (straight-line segments in the log plane), while other portions, chiefly at large x/d, depart significantly from this form.

Figure 5 shows that wave shape is affected by body nose shape in the nose region, but, as implied by blast wave theory (refs. 7 and 8), is nearly independent of nose shape farther downstream. Since all nose shapes approach congruence (flat face) as the drag coefficient approaches 1.8, the region over which the waves differ significantly decreases in size with increasing drag coefficient. It is worth noting in figure 5(c) that for the 1.3 drag coefficient cone, the front part of the wave was conical at the highest Mach number (initial slope of 1.0), but was curved at the two lowest Mach numbers (initial slope < 1.0), indicating incipient detachment.

Analytical Representation for Ellipsoids

Use of the machine program written to perform the stream-tube calculations of reference 4 requires an analytical representation of the shock-wave profile. An attempt was therefore made to obtain the best possible analytical

representation of the experimental profiles. The wave profiles for the ellipsoid family of nose shapes, being the most regular, were considered first.

The first approximation blast-wave prediction for shock-wave shape (refs. 7 and 8) is expressed as

$$\frac{R}{d} = 0.795\ C_D^{1/4} \left(\frac{x}{d}\right)^{1/2} \tag{1}$$

In figure 4, this would be represented by lines with a slope of 1/2 crossing the $x/d = 1.0$ line at $0.795\ C_D^{1/4}$. It can be seen that contrary to the blast-wave prediction the lines are not straight and the slope of the initial portion varies with both Mach number and drag coefficient. Seiff and Whiting, in references 4 and 5, modified equation (1) to the form

$$\frac{R}{d} = \text{constant} \left(\frac{x}{d}\right)^{n} \tag{2}$$

which again is a straight line in the log plane having a slope of n and the constant is the value of R/d at $x/d = 1.0$. Although useful over a range of x/d which depends on C_D and M_∞, this equation does not have the proper asymptotic behavior (finite slope as $x/d \rightarrow \infty$). An equation of hyperbolic form was selected since near the nose the equation reduces to the form of (2) and far downstream the slope is finite.

$$\frac{R}{d} = k\left[\left(\frac{x}{d}\right)^{1/n} + a\left(\frac{x}{d}\right)\right]^{n} \tag{3}$$

Equation (3) is a hyperbola if n is equal to 1/2. It was subsequently discovered that the second approximation blast-wave equation (ref. 8) can be written in this form where

$$\left.\begin{aligned} k &= \frac{(-\lambda_1)^{1/2}}{M_\infty} = \left(\frac{1.41}{M_\infty}\right)_{\gamma=1.4} \\ a &= \frac{C_D^{1/2}\ M_\infty^{2}}{-\lambda_1(4J_o/\gamma_\infty)^{1/2}} = \left(\frac{C_D^{1/2}\ M_\infty^{2}}{3.15}\right)_{\gamma=1.4} \\ n &= 1/2 \end{aligned}\right\} \tag{4}$$

and therefore predicts that the shock wave is a hyperbola. As shown in figure 4 the initial slopes are not, in general, 1/2, and it was therefore decided to obtain empirical fits of equation (3) to the data for the ellipsoids. The experimental data were fitted by a least squares routine and the resulting values of the constants k, a, and n are given in table I and plotted in figure 6. To clarify the physical meaning of these constants it

should be noted that k is the slope of the asymptote and n is the initial slope in the log plot. A value of n of 1.0 means that the initial portion of the wave is a cone while a value of zero would indicate a step function. There is no physical interpretation of a. It can be seen in figure 6 that k has the same variation with Mach number as a Mach line but increases with drag coefficient. No physical significance is attached to this increase. Rather, it is thought to indicate that the form of equation used is only an approximation to the correct form. The value of n is seen to decrease with both Mach number and drag coefficient and to vary appreciably from the value of 1/2 predicted by blast-wave theory. This is not surprising since the blast-wave theory assumes that the body has zero thickness.

The regular behavior of the constants k, a, and n, as shown in figure 6, suggested that correlations could possibly be found. Attempts to use the blast-wave parameters as a basis for correlation were unsuccessful; however, empirical correlations were found and the results reported in reference 9. For convenience the correlation equations are repeated below:

$$\left.\begin{aligned}
k &= \frac{1}{\sqrt{M_\infty^2 - 1}} + 0.057\, C_D^{1.35}\, M_\infty^{-0.0687} \\
a &= 0.56\left[C_D^{0.75}(M_\infty^2 - 1)\right]^{0.274+1.15\left[C_D^{0.75}(M_\infty^2-1)\right]^{-0.07}} \\
n &= \frac{0.646e^{-0.237\, C_D^{0.75}}}{\left(C_D^{0.5}\, M_\infty^2\right)^{0.034}}
\end{aligned}\right\} \qquad (5)$$

and are plotted in figure 6. The use of equations (3) and (5) has been found to represent the experimental wave ordinates within 4 percent for Mach numbers from 5 to 15.

Some justification for the use of these equations to Mach numbers as high as 20 may be found in figure 7. The symbols define the measured shock profiles of hemisphere models fired through still air at Mach numbers of 16.4 and 20.4. The curves were calculated by means of equations (3) and (5). Agreement is still within 4 percent at a Mach number of 20.4.

Analytical Representation for Cones and Sphere-Cones

The experimental waves for the cones and sphere-cones were divided into segments to which equations of parabolic form, hyperbolic form, or a form which plots as a circular arc in the log plane were fitted. It should be noted that the manner in which the segments join will affect the flow-field calculations. If there is a discontinuity in wave slope at the joint, there will be a discontinuity in the density and temperature profiles normal to the body. A discontinuity in the second derivative of the wave will cause a discontinuous slope in the density and temperature profiles. For the present

investigation, the constraint imposed on the analytic representations of the waves was that the ordinates and first derivatives must be continuous but that higher derivatives need not be.

Significance of Total Enthalpy as a Parameter

The present experimental program was conducted at total enthalpies far below those of flight in the atmosphere at the same Mach numbers. The question of the effect of total enthalpy on the shock-wave profiles is therefore of interest. Seiff suggested in reference 5 that at high Mach numbers, the shock-wave shape was primarily a function of total enthalpy rather than Mach number. Some conclusions can be drawn concerning this question if we refer again to the wave profiles in figure 7. Total enthalpy of the still-air shot at $M = 16.4$ was approximately four times that of the shots from which the correlations were obtained, and the density was about one-quarter of that of the other shots at comparable Mach numbers. One may conclude that the fourfold increase in total enthalpy had no significant effect on the wave shape. The solutions of reference 10 indicate that the variations in free-stream density have little effect on the shock-wave profiles. This conclusion is reinforced by the agreement of the experimental and predicted profiles at $M = 20.4$, where the total enthalpy for the experimental profile was approximately six times that of the tests from which the correlations were obtained. There is, of course, the possibility that at this Mach number, an error due to extrapolation of the correlation equations could mask an enthalpy effect if the two effects compensated one another. The experimental wave shape at $M = 20.4$ was also compared with the predictions of reference 5. The prediction based on Mach number was in good agreement, while that based on total enthalpy was not. The foregoing comparisons tend to indicate that Mach number is the important parameter rather than total enthalpy.

EVALUATION OF METHOD OF ANALYSIS

The computation method, as presented in reference 4 and hereinafter called the stream-tube method, is based on three main assumptions: (1) the flow along streamlines is isentropic between the bow-shock wave and the station being considered, (2) the flow is parallel to the vehicle axis, and (3) the shape of the pressure distribution along rays, normal to the vehicle axis between the body and the shock wave, is known. The actual pressure level is then found by an iterative procedure using conservation of mass and the entropy distribution as found from the shock-wave profile. The first of the above assumptions is valid for equilibrium flow if there are no embedded shock waves between the bow-shock wave and the station of interest and if there is no energy transport across streamlines. The second assumption restricts the method to the cylindrical portion of the vehicle and is thought to introduce only small error for the shapes considered. The key to success of the stream-tube method lies in assumption (3), and this will be explored further in the comparisons with method-of-characteristics solutions below.

In the present program, as in reference 4, it is assumed that the form of the pressure distribution normal to the body is that predicted by the first-approximation blast-wave analogy (ref. 7). A comparison of this distribution with that obtained from an equilibrium-air method-of-characteristics solution for a hemisphere cylinder at 20,000 feet per second is given in reference 4 and shows substantial agreement between the two methods. A further comparison with a method-of-characteristics solution (ref. 1) is given in figure 8 for a hemisphere cylinder at a Mach number of 7.7. Although the evaluation of assumption (3) is concerned primarily with the pressure distribution, density and velocity distributions are also shown. Included in figure 8(c) are experimental data by Kubota from reference 11. The method-of-characteristics solution represents the details of the field better than does the present method. At other stations both solutions are qualitatively similar except at the shoulder (fig. 8(a)), where the blast-wave pressure distribution is markedly different from that of the characteristics solution. The agreement for density and velocity is similar and tends to further justify assumption (2). The fact that the agreement between the two methods for the cases of figure 8 is not as good as that shown in reference 4 for a higher Mach number is thought to be due to the low Mach number of the present comparison. In reference 8, it was shown that the second-approximation blast-wave prediction gave good agreement with the data shown in figure 8(c); it might therefore be argued that the stream-tube method might be improved by the use of the second approximation. The difference between the first- and second-approximation blast-wave solutions is briefly discussed in appendix B, where it is shown that the second approximation is unrealistic for many conditions. Therefore all the computations herein reported utilized the first-approximation blast-wave pressure distribution.

The results of solutions by the method of characteristics (ref. 12) and the stream-tube method are compared further in figure 9 for the case of a hemisphere cylinder at 36,000 feet per second at 100,000 feet altitude (equilibrium air). The shock-wave profile required by the stream-tube method was taken from the solution of reference 12. It should be noted that great care was required in obtaining the analytical fit to the shock wave so that the correct pressure behind the shock wave was obtained. Although the shape of the pressure distribution curves are similar for the two methods, surface pressures disagree significantly for the more forward stations. Errors due to flow angularity near the shock wave (not accounted for in the stream-tube method) are possibly significant in this case.

All the above comparisons have been for hemisphere cylinders. To evaluate the method for other types of nose shape, a further comparison is made with unpublished calculations by Lomax (perfect gas method of characteristics) for a cone-sphere cylinder at a Mach number of 14.4 (fig. 10). The pressure distribution differs significantly for the most forward station but agrees in form for the other three stations. In addition, good quantitative agreement is obtained at $x/d = 2.2$ and 4.2. At $x/d = 7.7$, the slope of the shock wave (as shown by pressure behind the shock wave) differs significantly, resulting in poorer quantitative agreement. This illustrates the importance of good analytical fits to the experimental shock waves. Note that there is a knee in the pressure distributions from the characteristics solutions.

Since a change in the sign of the pressure gradient normal to the streamlines indicates a change in the direction of curvature of the streamlines, the characteristics solution indicates that the streamlines change from convex to concave in relation to the body in going from the body to the shock wave at the two forward stations. At $x/d = 4.2$, the streamlines would be concave, convex, and then concave again. It is not known at present if this is a realistic solution.

Although characteristics solutions are frequently considered to be exact, it should be pointed out that numerical errors can be significant. For example, for the above case, earlier calculations made with the linear entropy interpolation procedure of reference 1 washed out the constant-entropy part of the flow field (that part which came through the conical part of the shock wave) before it reached the cylinder. The program has since been changed to use a quadratic entropy-interpolation method and this procedure was used for the solution of figure 10. Thus it is well to keep in mind that while the equations are exact, the solutions are always subject to inaccuracies of this type.

In summary, the stream-tube method has been compared to method-of-characteristics solutions for hemisphere cylinders and for a 46° cone-sphere cylinder. Although the accuracy of the stream-tube method is limited by the assumption of the pressure distribution form, it has been shown to compare favorably with the characteristics solutions except near the nose ($x/d < 2$).

RESULTS AND DISCUSSION

The flow properties in the shock layer were computed for shock-wave stations 1, 2, 4, 8, and 16 body diameters for each model listed in table I. To relate these stations to body stations, the shock-wave stand-off distance must be subtracted from the shock-wave stations; for most conditions, the difference is unimportant. Calculations were attempted for all cases for equilibrium air at an altitude of 100,000 feet. Due to some interpolation problem in the machine use of the equilibrium-air tables, a few cases could not be solved for these conditions. In addition, solutions were obtained for the ellipsoid noses for ideal air ($\gamma = 1.4$) and for the hemisphere cylinder at Mach numbers of 10 and 15 for altitudes of 50,000 and 200,000 feet (see table below).

Altitude, ft	Pressure, lb/ft^2	Density, $slug/ft^3$	Temperature, $^{\circ}R$
50,000	243.6	$0.3639(10)^{-3}$	390.1
100,000	23.09	$.3211(10)^{-4}$	419.1
200,000	.475	$.6061(10)^{-6}$	457.1

Since changes in free-stream density and total enthalpy have little effect on the shock-wave shape, the same shock waves were used in the calculations for the hemisphere cylinder at the various free-stream conditions.

The calculations performed for this study yielded distributions of p/p_∞, q/q_∞, ρ/ρ_∞, T/T_∞, and V/V_∞ throughout the flow fields of the systematically selected bodies. The streamwise variations along the body surface are treated first and compared with the results of other studies; the flow properties between the surface and the shock wave are discussed subsequently. In each of these sections, the effects of changes in altitude, Mach number, nose-drag coefficient, and nose shape are considered independently. The effects of changes in gas properties (perfect and real gases) are also explored.

Surface Properties

Several authors have found that surface pressures on the cylindrical afterbody are independent of nose shape for a given Mach number and drag coefficient and can be correlated by the blast-wave parameter $(x/d)/M_\infty^2 C_D^{1/2}$ (cf. refs. 13 and 14). As shown in figure 11, a similar result was found in the present investigation. Note that all the configurations studied are represented in this figure. Also shown by the filled symbols are results from method-of-characteristics solutions from references 10 and 12 (hemisphere cylinders in equilibrium air). Although the variation of pressure ratio with the blast-wave parameter is similar for the two methods, the pressure-ratio levels are noticeably different. The greatest differences occur as the pressure ratios approach 1 and thus would not be likely to cause serious errors in estimating loads.

Also shown in figure 11 are the first and second blast-wave approximations for perfect air and the correlation curves (derived from perfect-air method-of-characteristics solutions) from reference 15 for $\gamma = 1.4$ and $\gamma = 1.2$. Except for pressures at stations closer than two diameters from the nose, it is evident that the pressure decays more slowly than predicted by the blast-wave analogy or the correlation curves of reference 15. It was suggested in reference 15 that surface-pressure ratios for various gases could be correlated with a modification of the blast-wave parameter which included a function of γ and that the stagnation-point value of γ should be used in the correlation. For the equilibrium-air method-of-characteristics solutions shown in figure 11, the stagnation-point value of γ is less than 1.25 for Mach numbers equal to or greater than 10. It can be seen that the equilibrium-air characteristics solutions agree better with the $\gamma = 1.4$ correlation equation than with the $\gamma = 1.2$ correlation. It therefore seems that the correlation method proposed in reference 15 does not predict the results obtained from equilibrium-air method-of-characteristics solutions.

In addition to the surface-pressure distribution, temperature at the edge of the boundary layer, dynamic pressure, and other quantities must also be known for many purposes. If the body supports a normal shock wave at the

nose, the entropy on the body streamline is not a function of body shape or drag coefficient but of the free-stream conditions only. It has previously been shown that pressure on the afterbody is independent of the nose shape. Since all other flow properties are uniquely determined by entropy and pressure, these other properties are also independent of nose shape for bodies which support a normal shock wave.

Typical variations of pressure, temperature, density, and dynamic pressure along the body are shown in figure 12. In general, all properties decrease with increasing x/d but the details are functions of the gas thermodynamic properties. In particular, the temperature ratios decrease with increasing x/d more slowly for equilibrium air than for a perfect gas as a result of the increased number of modes of energy storage in equilibrium air as compared to a perfect diatomic molecule. An illustration of this fact can be obtained by constructing temperature - pressure diagrams for these conditions for an isentropic expansion from the stagnation conditions. As an additional interesting feature, it will be found that the equilibrium-air temperature is sometimes higher than that for perfect air at the lower pressures. This result can be seen in figure 12. Note that the dynamic pressure ratio is, in general, lower for equilibrium air than for a perfect gas. Except for surface-pressure ratios, which do not vary appreciably with gas properties (fig. 11), attempts to correlate the properties were unsucessful. These properties can, however, be readily calculated. The surface pressure from figure 11 and the calculated entropy behind the appropriate shock wave can be used to find all other properties from the thermodynamic charts of reference 16 or 17. To aid in making this calculation rapidly, the entropy in equilibrium air behind a normal shock wave as a function of velocity and altitude is presented in figure 13. For this figure, the variation of pressure and density with altitude was taken from reference 18. To use this chart for bodies with conical shock waves, the appropriate velocity is, of course, the velocity normal to the shock wave.

The variations of pressure, temperature, density, and dynamic-pressure ratios on the body surface with drag coefficient and free-stream Mach number for one station ($x/d = 4.0$) are shown in figure 14. In general, pressure and temperature ratios increase with increases in both drag coefficient and Mach number, while density and dynamic-pressure ratios increase with increasing drag coefficient and decrease with increasing Mach number. Again, it is evident that the variations for equilibrium air are not so regular as those for a perfect gas.

Although the information contained in figure 14 was obtained from solutions for ellipsoid-nosed bodies, the information is valid for any bodies which have detached bow waves at the nose. For conical-nosed bodies, on the other hand, the pressure ratio along the body is as shown in figure 11, but the entropy on the surface streamline is lower than for the ellipsoids. The surface values of temperature, density, and dynamic-pressure ratios for cones are compared, for $x/d = 4.0$, to those for ellipsoids in figure 15. For the cones with low drag coefficients, temperature ratios at the afterbody surface are much lower than for the ellipsoids, and density and dynamic-pressure ratios are much higher. The cone with a drag coefficient of 1.3 had a detached shock wave for Mach numbers of 5 and 10. Therefore the surface

properties are approximately equal to those for the corresponding ellipsoid. At a Mach number of 15, however, the shock wave was attached and the surface properties differed from those for the ellipsoid. Note that the dynamic-pressure ratio increases slightly with drag coefficient for the ellipsoids because of the increasing static-pressure ratio but decreases rapidly with increasing drag coefficient for the cones until the cone angle for shock-wave detachment is reached.

Surface values of temperature, density, and dynamic-pressure ratios for the hemisphere cylinder ($x/d = 4.0$) have been replotted in figure 16 to show more clearly the variations with Mach number. The comparisons at a Mach number of 35.9 for a perfect gas and for altitudes of 50,000 and 200,000 feet were obtained using the entropy for 36,000 feet per second at the appropriate altitude and the static-pressure ratio from reference 12. The variation of dynamic-pressure ratios shows two important results which bear on the stability of flare-stabilized bodies. First, dynamic-pressure ratio, and therefore flare effectiveness, decreases with increasing Mach number (ref. 19), and second, dynamic-pressure ratios are approximately 25 to 30 percent lower in equilibrium air than in perfect air over the high Mach number range. This suggests that high Mach number tests at low total enthalpy could overpredict the stability of flared bodies.

From these results, one is led to study the effects of nonequilibrium flow on the dynamic-pressure ratio. A brief comparison was made using the following assumptions: the surface-pressure ratio is the same as in the equilibrium case at the same Mach number, the flow is in equilibrium up to the stagnation point, and the chemistry and vibrational energy are frozen in the flow over the afterbody at the stagnation-point values. When the shock-wave solution for 100,000 feet altitude was used, the dynamic-pressure ratio was found to be everywhere greater than the perfect-air curve in figure 16. Since the assumption of unchanged surface-pressure ratio is subject to question (ref. 20), the pressure ratio (for $V = 36,000$ ft/sec) was varied from 5 to 20 ($p/p_\infty = 14$ nominal) with the consequent variation of the dynamic-pressure ratio from 0.140 to 0.282 ($q/q_\infty = 0.115$ at $p/p_\infty = 14$ in equilibrium air). Thus frozen flow, as well as perfect-gas flow, gives higher dynamic-pressure ratios than equilibrium flow along the afterbody, again suggesting that the stability of flared bodies may be sensitive to flow chemistry.

Flow Properties Between Surface and Shock Wave

Since the basic assumption of the computation method was that the form of the pressure distribution between the body and shock wave is known, it is necessary only to consider the boundary values. The surface pressures have been discussed previously (fig. 11) and certain facts about the pressure behind the shock wave can be determined from the shock waves previously presented. Since the pressure increase across a shock wave is approximately the same in equilibrium air as in perfect air and the shock-wave shape is relatively independent of nose shape downstream of the nose, the pressure

ratio behind the shock wave is also independent of altitude and nose shape. Further, it can be shown that the pressure behind the shock wave has approximately the same parametric variation as the surface pressure. The pressure distributions are therefore not shown since this would involve simply repetition of the assumed distribution with end points whose values can be obtained from the information previously given. For properties other than pressure, however, the values in the shock layer vary with the entropy distribution and these variations will be discussed in more detail below.

First the effects of altitude on the radial profiles of temperature, density, and dynamic-pressure ratios are shown in figure 17. In the outer portion of the shock layer where the flow has passed through a relatively weak wave, the altitude effects are small. Near the body however, the effects are sizable, particularly on the temperature ratios. As previously shown with the effects on surface properties, these results do not lend themselves to generalizations but must be calculated for each situation.

To illustrate the effects of Mach number, drag coefficient, and nose shape on the flow fields, a number of calculations for equilibrium air at 100,000 feet altitude have been made. The effects of Mach number on the flow properties in the shock layer for the 0.5 and 1.8 drag-coefficient ellipsoids are shown in figure 18. Note that, as previously shown, the temperature near the body decreases with increasing x/d. However, at some distance away from the body, temperature increases with increasing x/d for the higher Mach numbers. This is not to say that temperature increases along a streamline but that, despite the assumption of purely axial flow at any station, the streamlines are diverging with respect to the body. The general effects of Mach number are that both the magnitude of the changes in flow properties in the high entropy layer near the body and the size of this layer are increased with increasing Mach number.

The effects of variations in drag coefficient on the flow properties are shown in figure 19. In general, increasing drag coefficient increases the shock-layer thickness and also the thickness of the high entropy layer. The shape of the outer portion of the profiles is not appreciably changed by changes in drag coefficient.

At higher Mach numbers, the recombination reactions become important in the region of interest of this report as shown in figure 20. In this figure, there is an irregularity in the temperature profile in the region near $T/T_\infty = 14.0$. This results from the recombination of oxygen. At the densities for this condition, the oxygen is almost completely dissociated near the body but is almost completely combined for temperatures below 12 times free-stream temperature. Since dissociation temperatures depend on the density, irregularities in the temperature profiles such as this must vary in position with both Mach number and altitude.

The effects of changes in nose shape are shown in figure 21. As previously explained, changes in the nose shape for a given drag coefficient have little effect on the surface properties if the bow wave is detached.

Large differences were, however, found between bodies having attached conical shock waves and those having detached shock waves (fig. 15). In the flow field along normals to the body, the situation is more complicated and any change in the entropy distribution (shock-wave shape) produces a corresponding change in the distribution of flow properties. With conical shock waves, a region of essentially constant properties exists near the body which corresponds to that part of the flow which came through the conical part of the shock wave. For the sphere-cones, a similar region of essentially constant properties exists at a distance away from the body - again that part of the flow which came through the straight part of the shock wave. For a drag coefficient of 1.3, the shock waves are not greatly different for the three types of noses (fig. 5(c)) and neither are the flow fields. Since the body shapes approach congruence as drag coefficient approaches 1.8, the flow fields must also display the same trend. Rather large differences are seen in the flow fields of bodies with a drag coefficient of 0.9 as would be expected from the variation in shock-wave shapes (fig. 5(b)). For a drag coefficient of 0.5, the sphere-cone shock wave is again approaching that of the ellipsoid (fig. 5(a)) and therefore only small differences are seen in the flow fields for these bodies. The cone nose, however, now supports a very weak shock wave and there are large differences between the flow fields for the conical noses and those for the other noses. For all drag coefficients, the outer part of the flow field is little affected by changes in nose shape.

SUMMARY OF RESULTS

A systematic study has been made of the effects of changes in Mach number, altitude, nose-drag coefficient, and nose shape on the flow fields over the afterbodies of blunt-nosed cylinders traveling at hypersonic speeds.

It was shown that the variations in surface-pressure distributions were similar to those predicted by blast-wave theory; that is, except in the nose region, they were primarily functions of nose-drag coefficients and Mach number with only small influences of nose shape. The blast-wave theory is not, however, quantitatively accurate.

The rate of decay of surface pressure with x/d was found to be different in equilibrium air from that predicted by blast-wave theory or by method-of-characteristics solutions for perfect gases.

Surface values of temperature, density, and dynamic-pressure ratios could not be correlated but could be readily computed by means of the surface-pressure correlation data and the entropy behind the appropriate shock wave.

The thickness of the high entropy layer near the body was found to increase with both Mach number and drag coefficient. At high drag coefficients, the entropy distribution was relatively insensitive to nose shape. However, at low drag coefficients, the entropy for conical bodies was low in

this region compared to that for bodies with detached shock waves. Correspondingly large differences were found for temperature, density, and dynamic pressure ratios.

Surface-pressure ratios and shock-wave shape were found to be insensitive to changes in altitude. Temperature, density, and, to a lesser extent, dynamic-pressure ratios were found to vary appreciably with changes in altitude.

Ames Research Center
National Aeronautics and Space Administration
Moffett Field, Calif., Feb. 7, 1964

APPENDIX A

MEASUREMENT OF SHOCK-WAVE PROFILES

Shock-wave profiles for the previously described experimental program (table I, figs. 1 and 2) were obtained from shadowgraph pictures taken with two types of shadowgraph systems and a sample of each is shown in figure 3. Since, in general, the models were not at zero angle of attack in any of the pictures, the following data-analysis procedure was adopted to minimize angle-of-attack effects on the data. For each test, data were taken from two orthogonal views of the model at the two stations having the smallest resultant angle of attack. The x axis was selected to be parallel to the reference wire (located below the model in fig. 3(a) and above the model in fig. 3(b)) so as to bisect the shock wave near the downstream edge of the picture. Flight-path angle with respect to this reference wire was less than 0.2°. Because of the model angle of attack, the x axis did not necessarily pass exactly through the stagnation point. The origin of the coordinate system was then set so that the R axis passed through the most forward part of the wave. Measurements of R were then made on both sides of the x axis for many values of x. The resulting wave coordinates were made dimensionless with respect to the model diameter and plotted in both linear and logarithmic plots. Representative data are shown in the logarithmic form in figure 22. Each of the shadowgraphs for a test is represented by a different symbol and the spread between like symbols at the same value of x/d is indicative of the angle-of-attack effects. The shock-wave ordinate at zero angle of attack is considered to be the average of the data points at a given station.

APPENDIX B

BLAST-WAVE PRESSURE DISTRIBUTION

In the blast-wave theory, the solution may be constructed in a power series expansion of $1/M_R^2$, where $M_R = M_\infty \tan \theta$. (The reader is referred to reference 8 for a discussion of the blast-wave theory.) The first approximation blast-wave solution retains only the zeroth power of $1/M_R^2$ and the second approximation retains the zeroth and first power. For the data of figure 8(c), $M_R \approx 2.1$, which is too low for the first approximation to be valid. It was shown in reference 8 that there was good agreement between the data of figure 8(c) and the prediction of the second approximation. It was therefore thought that using the second-approximation blast-wave pressure distribution might improve the stream-tube method. For radial Mach numbers (M_R) much below 2.5, however, the form of the pressure distribution immediately behind the shock wave proved to be unreasonable (fig. 23) in comparison to the predictions of more exact theories (figs. 8-10). As shown in figure 24, the range of applicability of the method (region to the left of the appropriate line) would be severely limited if the requirement $M_R \geq 2.5$ or even $M_R \geq 2.0$ were imposed. Therefore, it was decided to retain the simplicity of the first approximation. The pressure distribution predicted by the first approximation is approximately that shown for a radial Mach number of 10.

REFERENCES

1. Inouye, Mamoru, and Lomax, Harvard: Comparison of Experimental and Numerical Results for the Flow of a Perfect Gas About Blunt-Nosed Bodies. NASA TN D-1426, 1962.

2. Gravalos, F. G., Edelfelt, I. H., and Emmons, H. W.: The Supersonic Flow About a Blunt Body of Revolution for Gases at Chemical Equilibrium. Ninth Annual International Astronautical Congress; Proceedings. Amsterdam, vol. 1, Aug. 25-30, 1958, pp. 312-32.

3. Vaglio-Laurin, Roberto, and Trella, Massimo: A Study of Flow Fields About Some Typical Blunt-Nosed Slender Bodies. PIBAL Rep. 623, AFOSR 2, Polytechnic Inst. of Brooklyn, Dec. 1960.

4. Seiff, Alvin, and Whiting, Ellis E.: Calculation of Flow Fields From Bow-Wave Profiles for the Downstream Region of Blunt-Nosed Circular Cylinders in Axial Hypersonic Flight. NASA TN D-1147, 1961.

5. Seiff, Alvin, and Whiting, Ellis E.: A Correlation Study of the Bow-Wave Profiles of Blunt Bodies. NASA TN D-1148, 1962.

6. Ames Research Staff: Equations, Tables, and Charts for Compressible Flow. NACA Rep. 1135, 1953.

7. Lin, Shao-Chi: Cylindrical Shock Waves Produced by Instantaneous Energy Release. Jour. Appl. Phys., vol. 25, no. 1, Jan. 1954.

8. Lukasiewicz, J.: Hypersonic Flow-Blast Analogy. AEDC-TR-61-4, 1961.

9. James, Carlton S., and Terry, James E.: Shock-Wave Profiles Over Ellipsoidal-Nosed Bodies in Hypersonic Flow. Jour. Aerospace Sci., vol. 29, no. 9, Sept. 1962, pp. 1128-9.

10. Fitzgibbon, S. A.: Shock Profiles and Pressure Distributions from Flow Fields Around a Hemi-sphere Cylinder. G. E. PIR 8152-005, 1961.

11. Kubota, Toshi: Investigation of Flow Around Simple Bodies in Hypersonic Flow. GALCIT Memo. 40, 1957.

12. Edsall, R. H.: Calculation of Flow Fields About Blunt Bodies of Revolution Traveling at Escape Velocity. ARS 2492-62, 1962.

13. Van Hise, Vernon: Analytical Study of Induced Pressure on Long Bodies of Revolution With Varying Nose Bluntness at Hypersonic Speeds. NASA TR R-78, 1960.

14. Mueller, James N., Close, Willian H., and Henderson, Arthur, Jr.: An Investigation of Induced-Pressure Phenomena on Axially Symmetric, Flow-Alined Cylindrical Models Equipped With Different Nose Shapes at Free-Stream Mach Numbers From 15.6 to 21 in Helium. NASA TN D-373, 1960.

15. Kuehn, Donald N.: Experimental and Theoretical Pressures on Blunt Cylinders for Equilibrium and Nonequilibrium Air at Hypersonic Speeds. NASA TN D-1979, 1963.

16. Moeckel, W. E., and Weston, Kenneth C.: Composition and Thermodynamic Properties of Air in Chemical Equilibrium. NACA TN 4265, 1958.

17. Feldman, Saul: Hypersonic Gas Dynamic Charts for Equilibrium Air. Avco Res. Rep. 40, 1957.

18. Anon.: U. S. Standard Atmosphere, United States Committee on Extension to the Standard Atmosphere. U. S. Govt. Printing Office, Washington, 1962.

19. Seiff, Alvin: Secondary Flow Fields Embedded in Hypersonic Shock Layers. NASA TN D-1304, 1962.

20. Geiger, R. E.: Some Exploratory Pressure Measurements on a Blunt Plate With a Non-Equilibrium Flow Field. AIAA 63-440, 1963.

TABLE I.- TEST CONDITIONS

Nose	C_D	M_∞	Re, million	T_∞, °R	ρ_∞, slug/ft^3	Least squares fit of equation (3) to experimental shock wave		
						k	a	n
Cone	0.5	5.54	1.60	526.4	0.002364			
	.5	9.59	1.64	187.5	.000938			
	.5	14.60	2.61	186.8	.000942			
	.9	5.27	1.57	517.4	.002422			
	.9	10.07	1.69	190.0	.000926			
	.9	14.80	2.49	187.1	.000918			
	1.3	5.08	1.46	531.4	.002352			
	1.3	9.76	1.73	188.6	.000970			
	1.3	15.19	2.56	188.9	.000927			
Ellipse	.5	4.54	1.28	531.4	.002315	0.254	11.8	0.510
	.5	9.75	1.63	191.8	.000924	.120	54.3	.488
	.5	12.96	2.06	198.0	.000894	.093	94.6	.480
	.9	5.00	1.44	530.4	.002353	.255	21.5	.465
	.9	9.56	1.62	183.5	.000916	.145	77.0	.444
	.9	14.40	2.40	189.3	.000917	.112	151.5	.432
	1.3	4.73	1.38	522.4	.002378	.291	27.5	.432
	1.3	9.56	1.66	187.9	.000954	.176	97.4	.410
	1.3	14.80	2.47	191.5	.000921	.135	196.0	.402
	1.8	4.64	1.36	521.4	.002389	.340	34.3	.393
	1.8	9.17	1.48	195.1	.000907	.214	117.7	.378
	1.8	14.16	2.45	187.1	.000944	.174	221.0	.370
	.9	16.4	.25	529.7	.000248			
	.9	20.4	.20	540.7	.000152			
Sphere-cone	.5	4.92	1.36	535.4	.002296			
	.5	10.30	1.70	192.2	.000918			
	.5	14.34	2.39	191.5	.000923			
	.9	4.90	1.41	529.4	.002338			
	.9	10.28	1.83	187.9	.000974			
	.9	15.10	2.55	188.2	.000928			
	1.3	5.14	1.49	523.4	.002370			
	1.3	10.52	1.79	188.6	.000933			
	1.3	14.60	2.40	192.2	.000923			

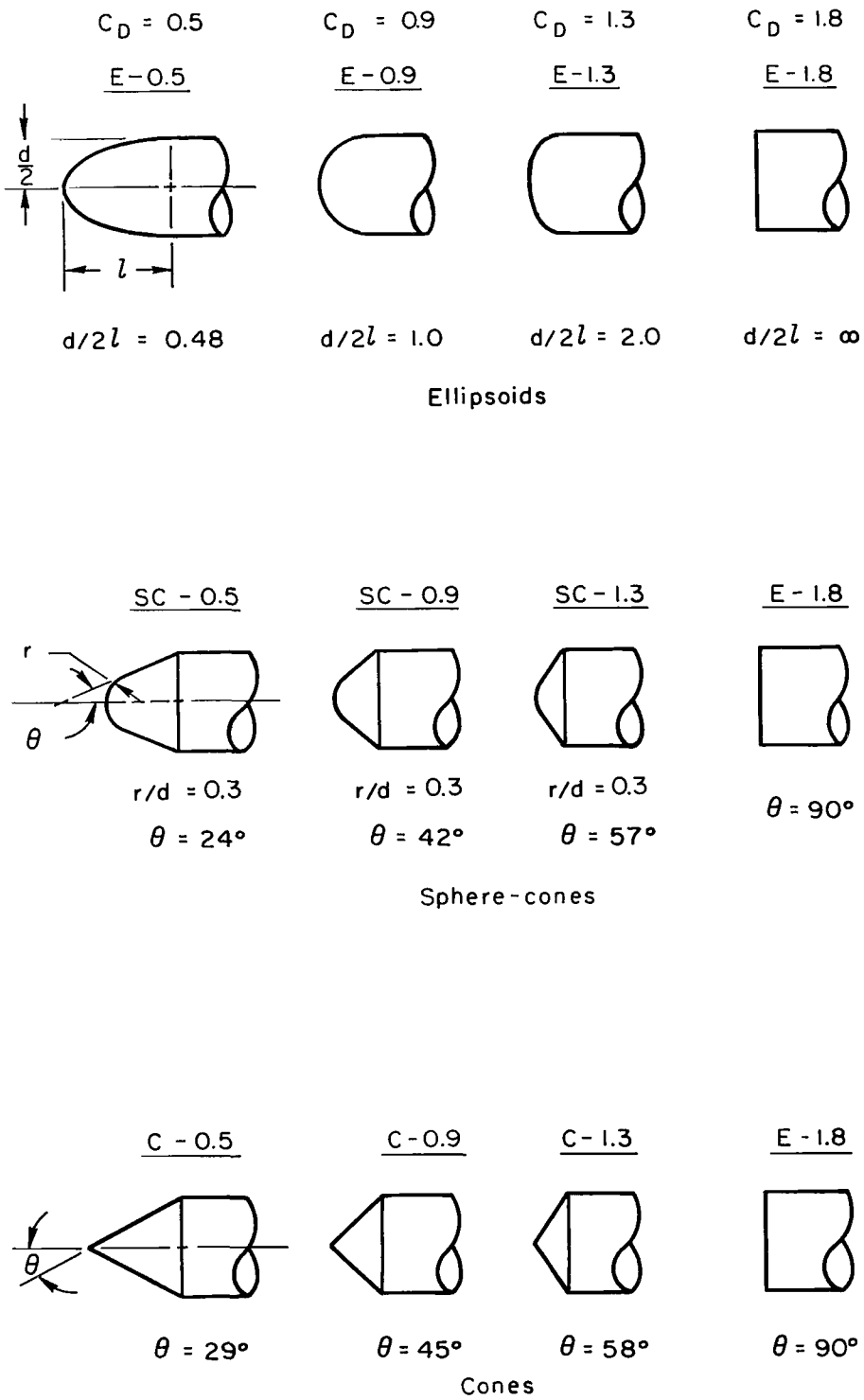

Figure 1.- Nose shapes of models tested.

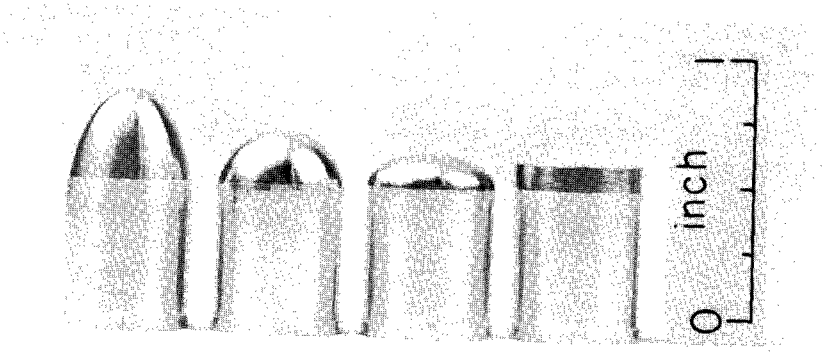

A-27691

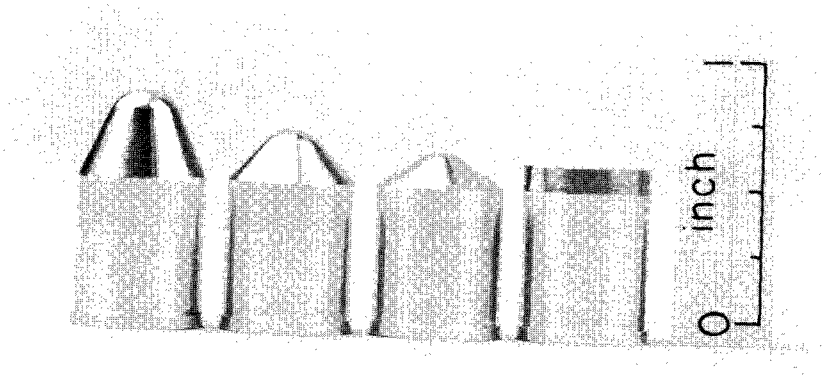

A-27690

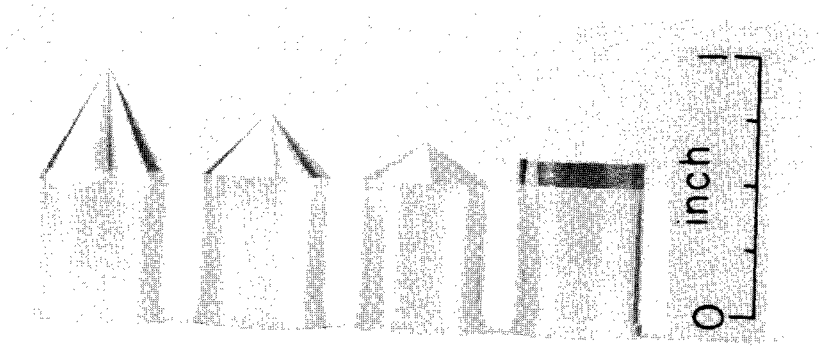

A-27689

Figure 2.- Test models.

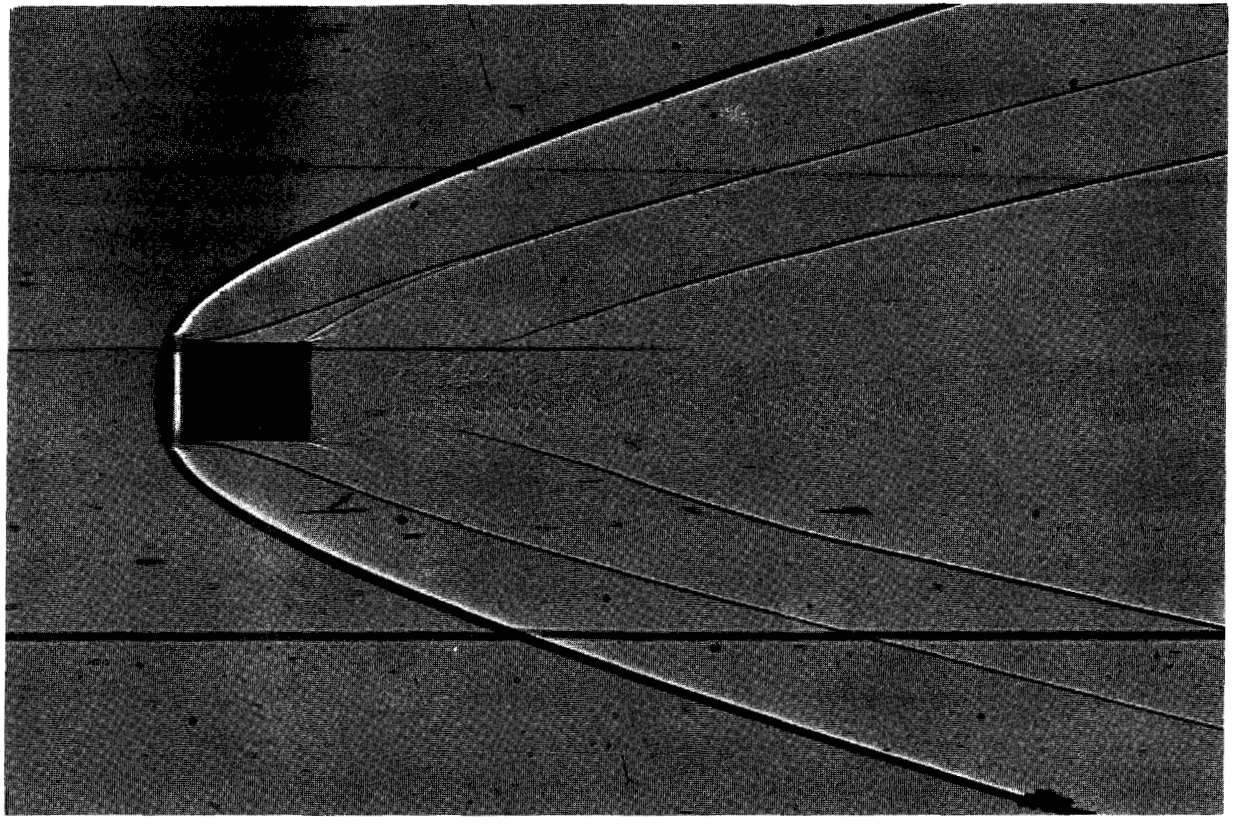

(a) E-1.8, $M_\infty = 4.64$

Figure 3.- Representative shadowgraphs.

(b) SC-1.3, $M_\infty = 10.3$

Figure 3.- Concluded.

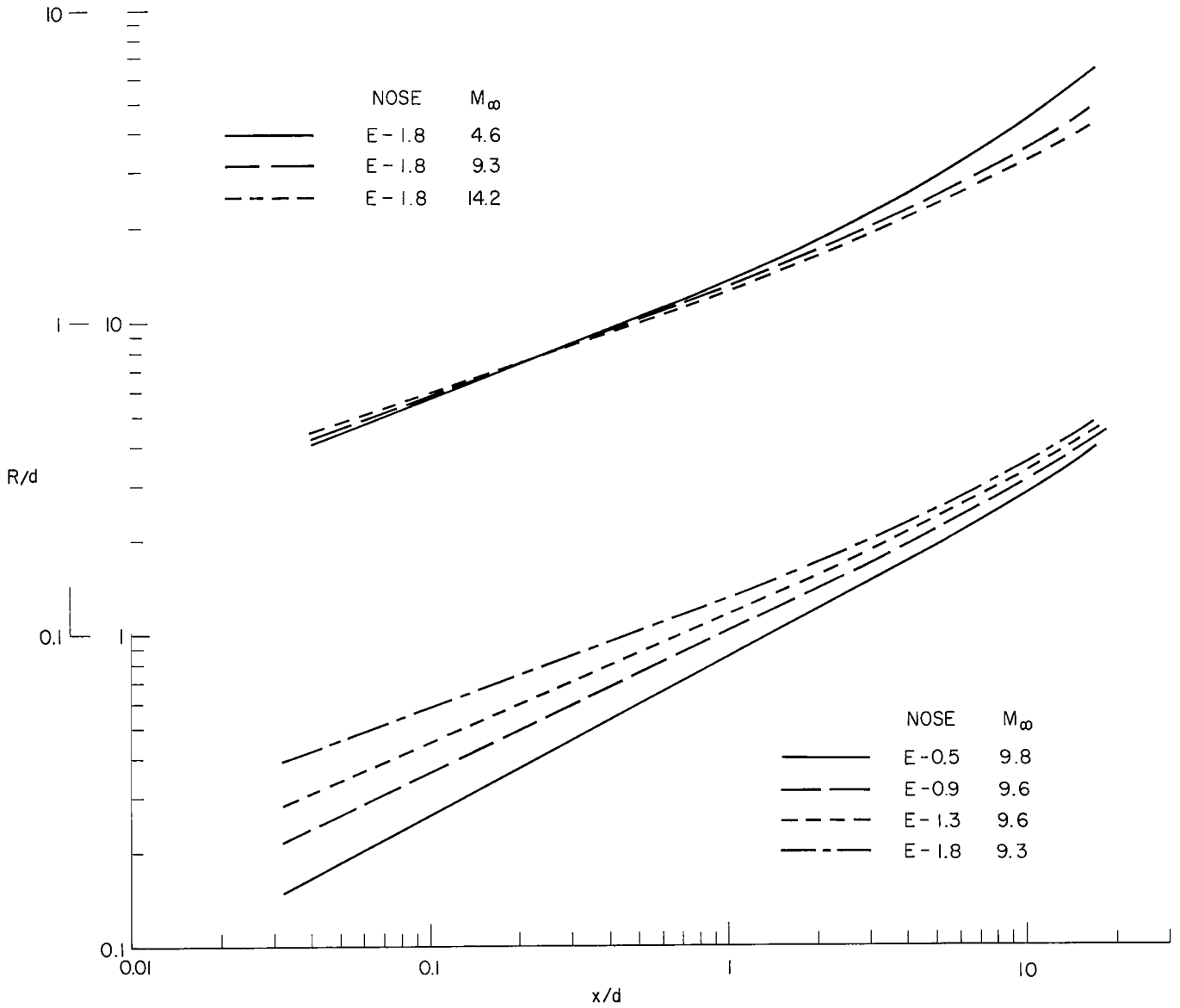

Figure 4.- Variation in shock-wave shape with Mach number and drag coefficient for ellipsoid-nosed-cylinders.

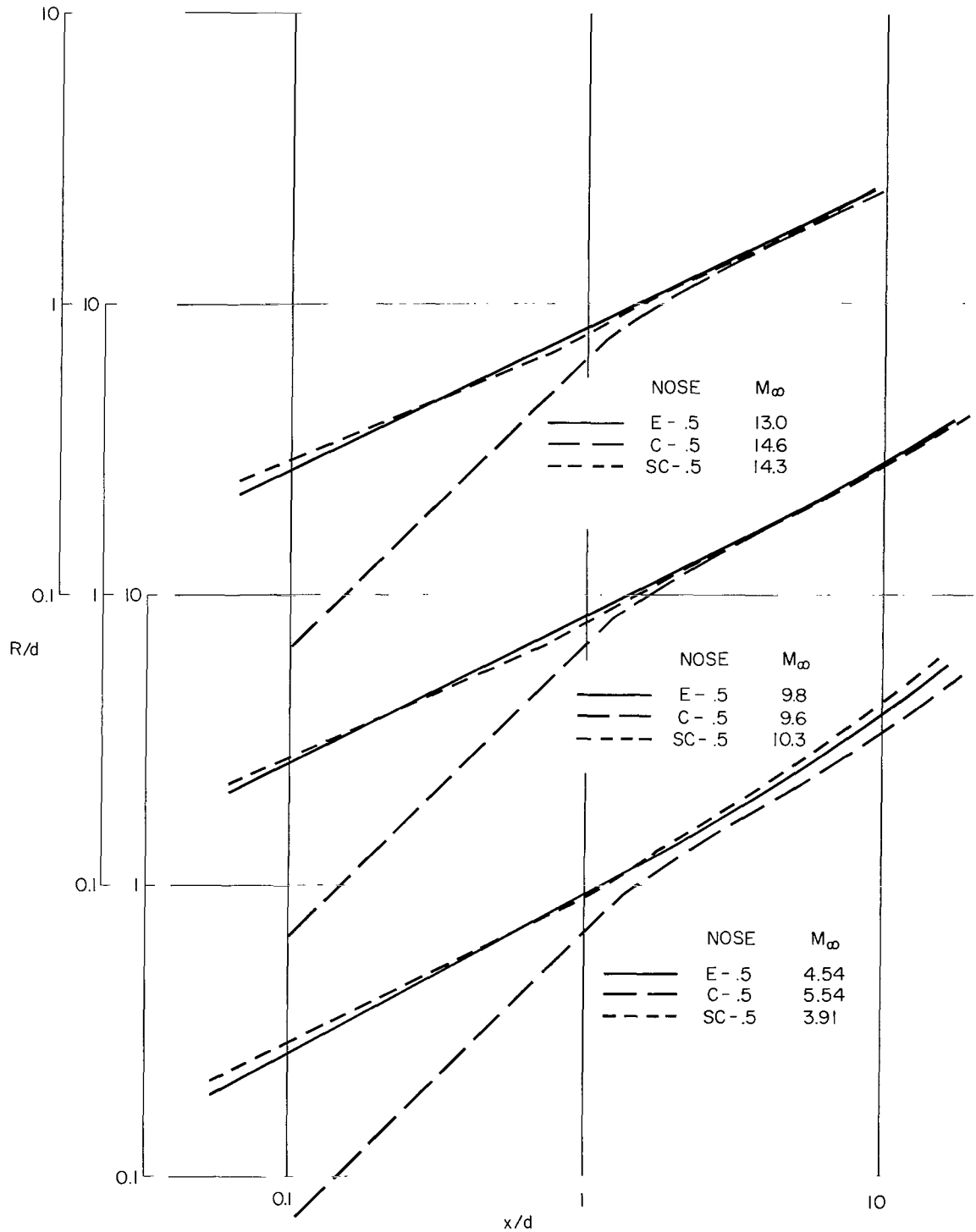

(a) $C_D = 0.5$

Figure 5.- Experimental shock-wave profiles.

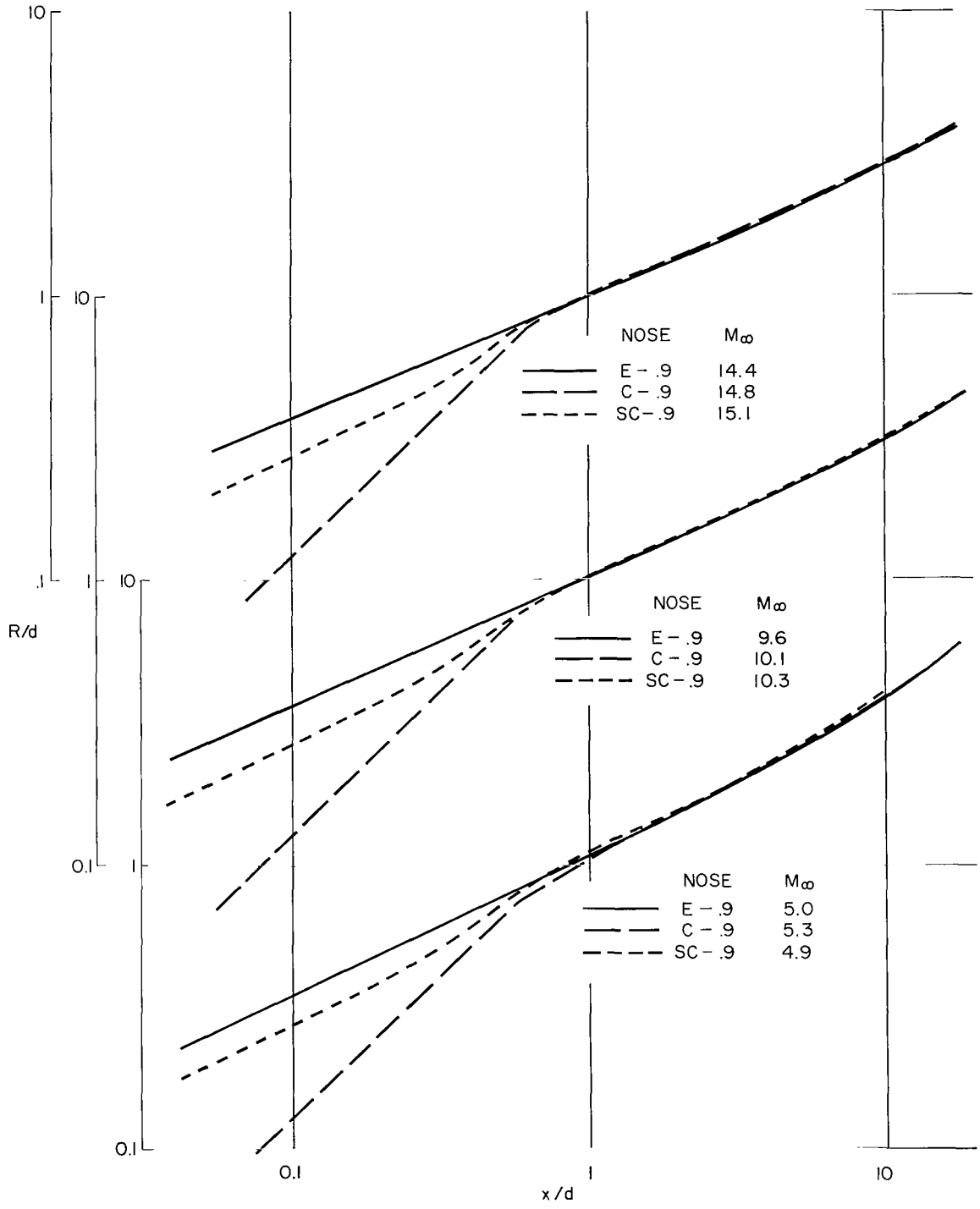

(b) $C_D = 0.9$

Figure 5.- Continued.

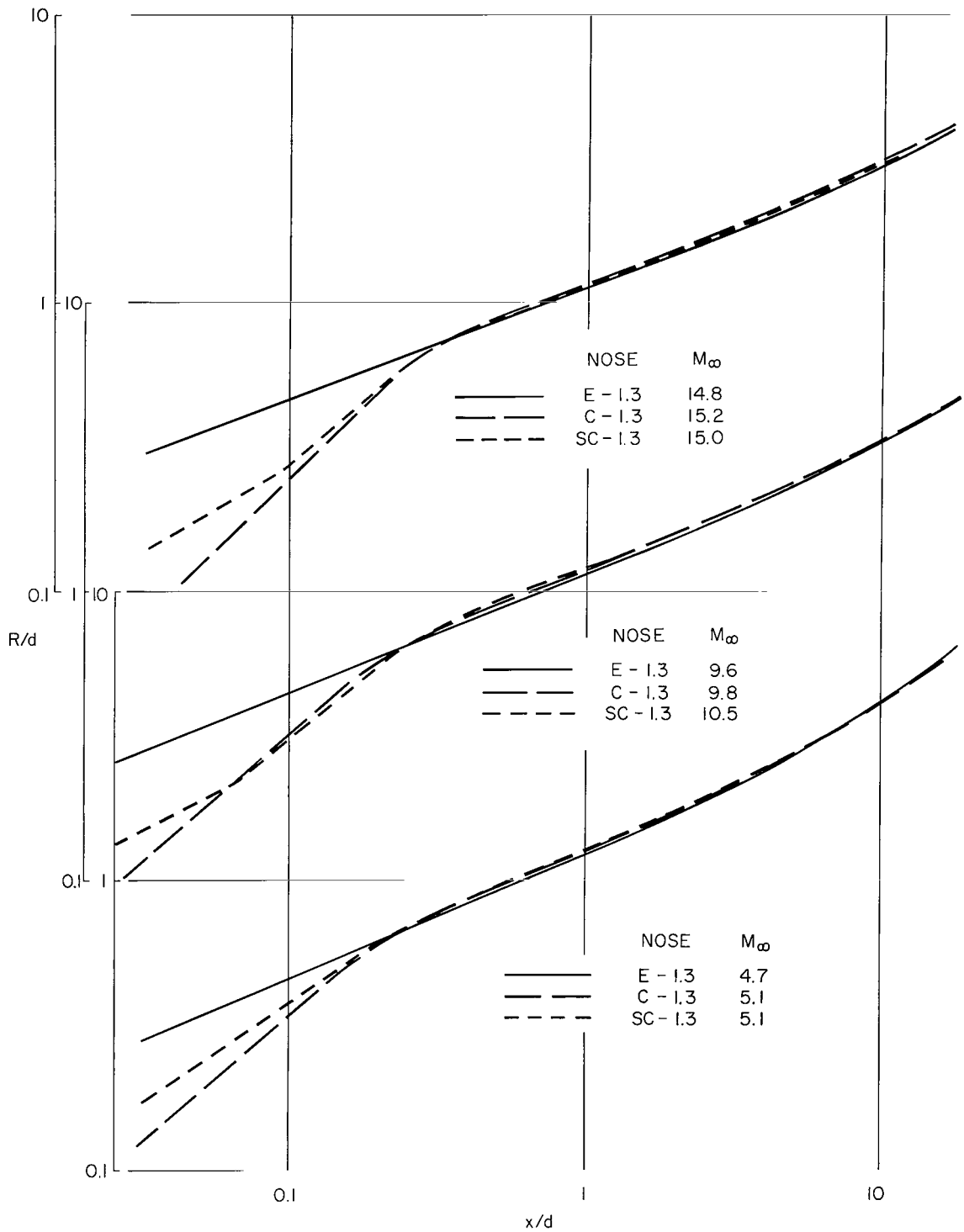

(c) $C_D = 1.3$

Figure 5.- Concluded.

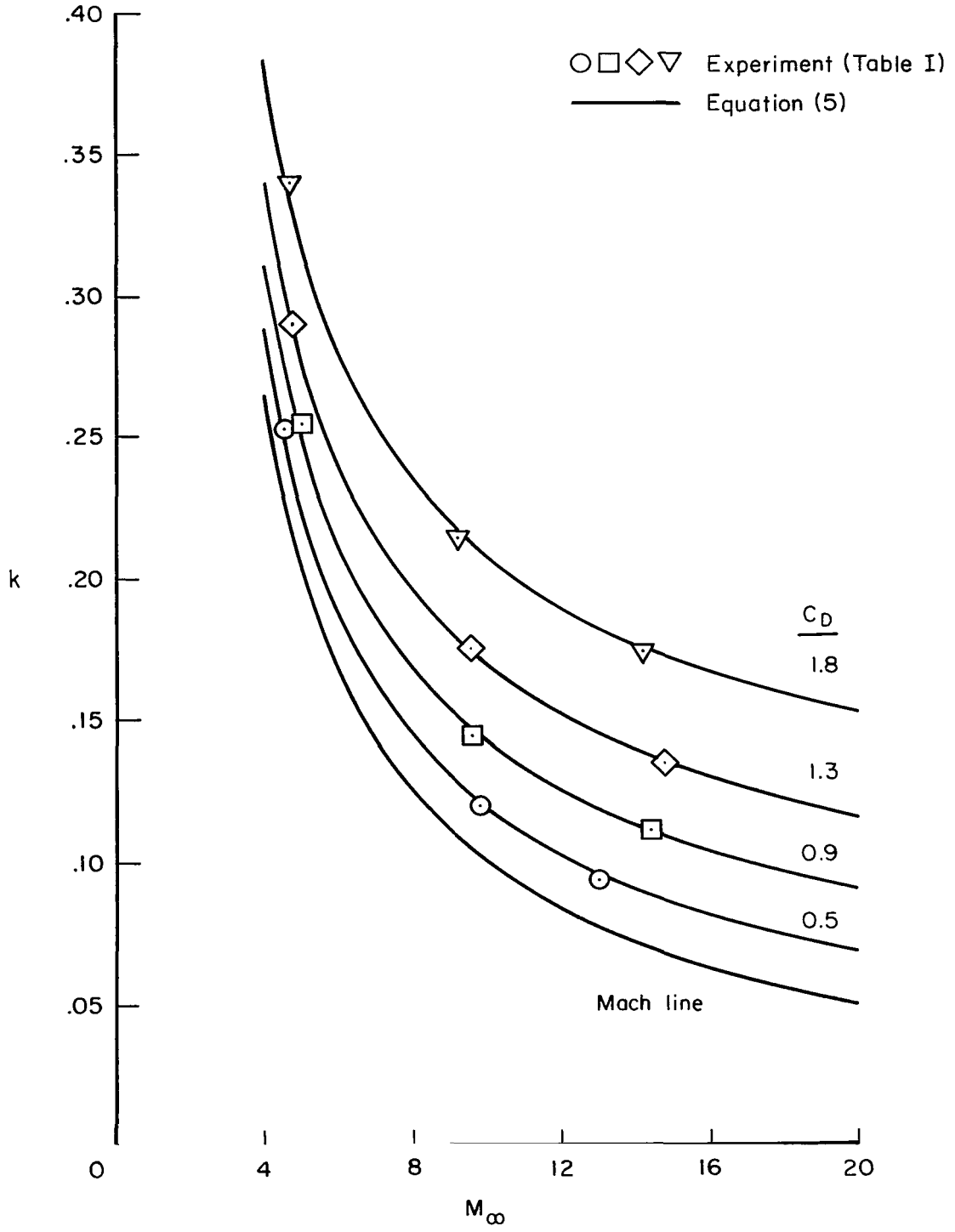

(a) k

Figure 6.- Coefficients defining shock-wave shape for use in equation (3).

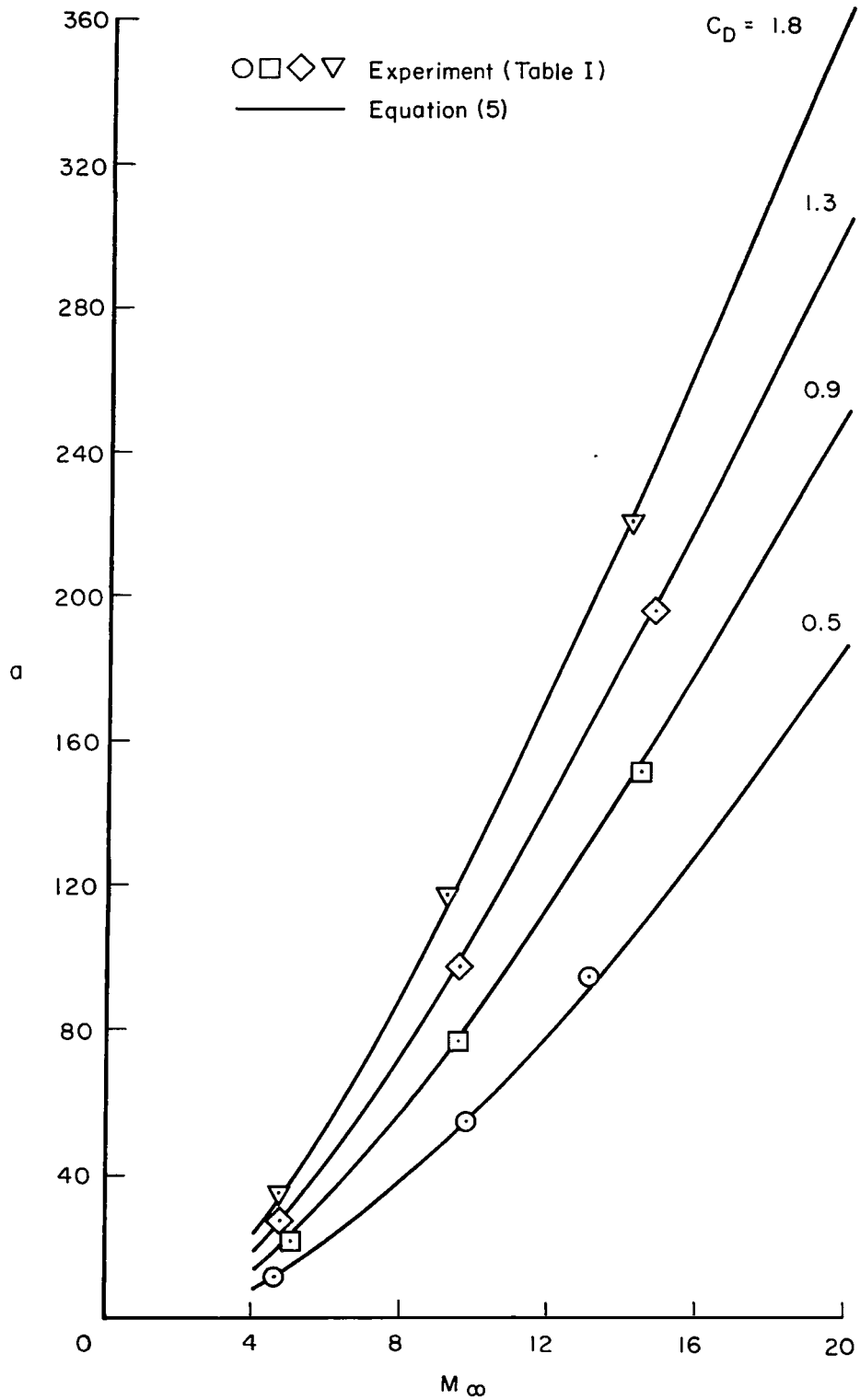

(b) a

Figure 6.- Continued.

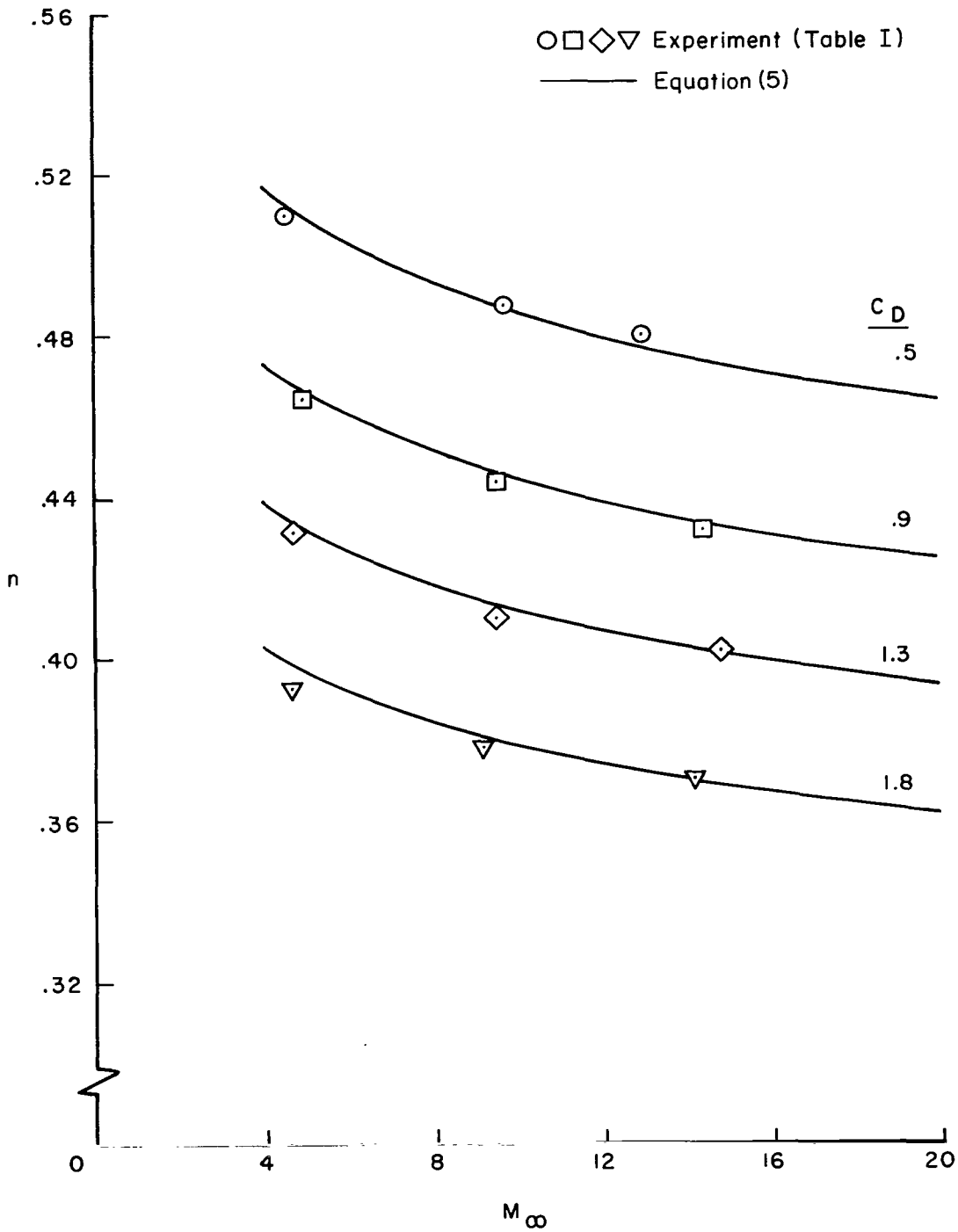

(c) n

Figure 6.- Concluded.

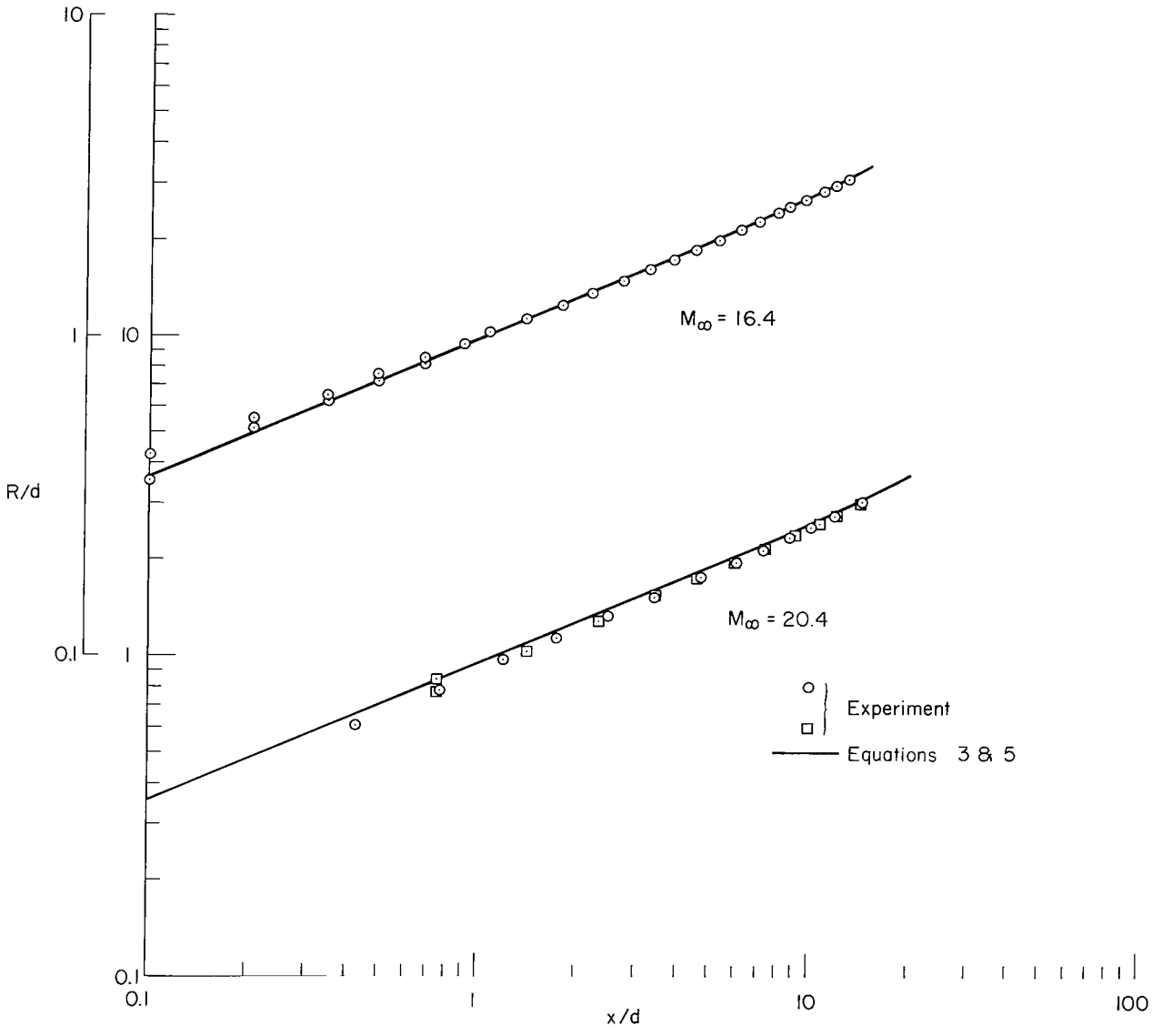

Figure 7.- Shock-wave profiles over hemisphere-cylinders.

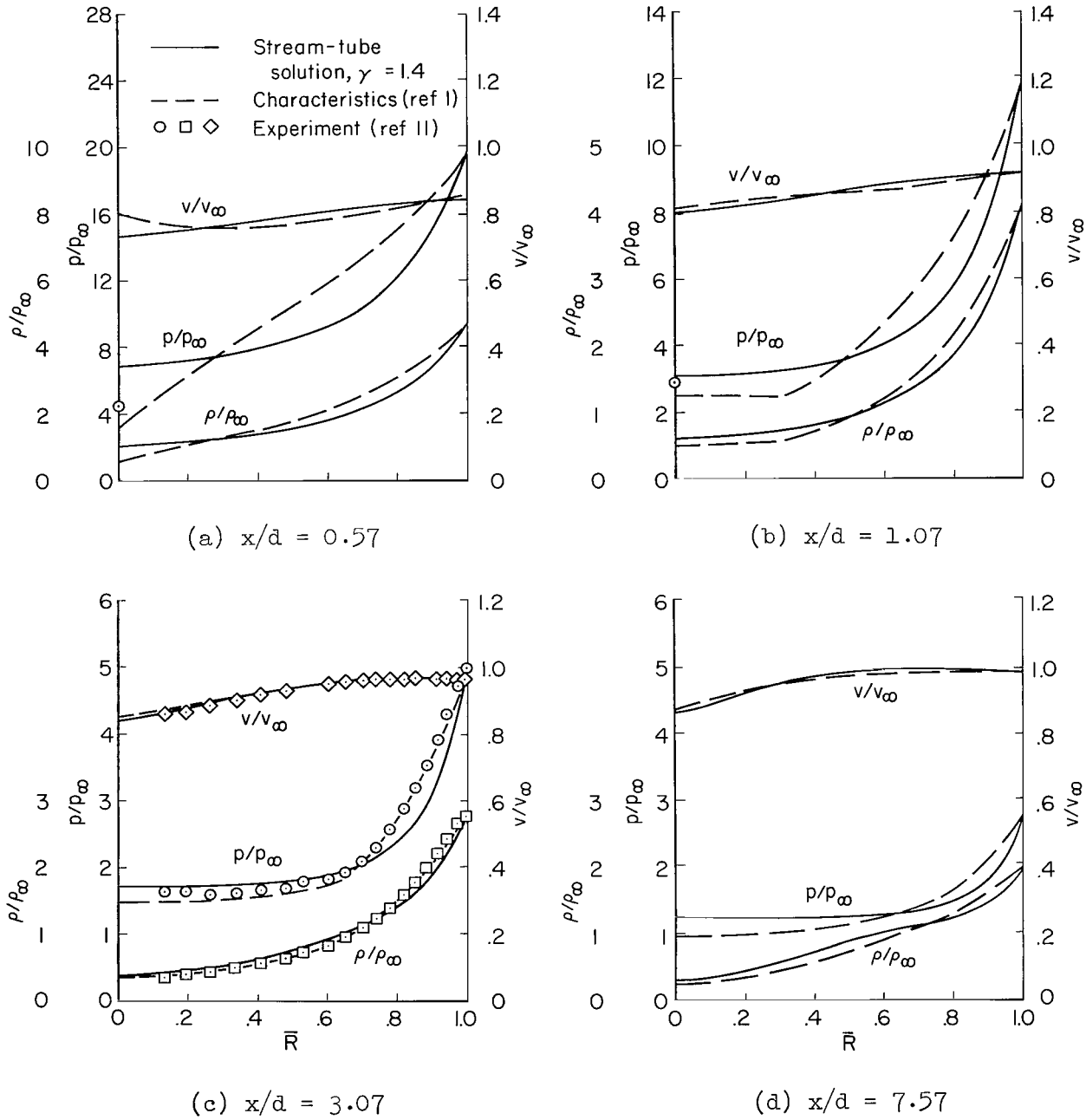

Figure 8.- Comparison of calculated flow fields over a hemisphere-cylinder at $M_\infty = 7.7$.

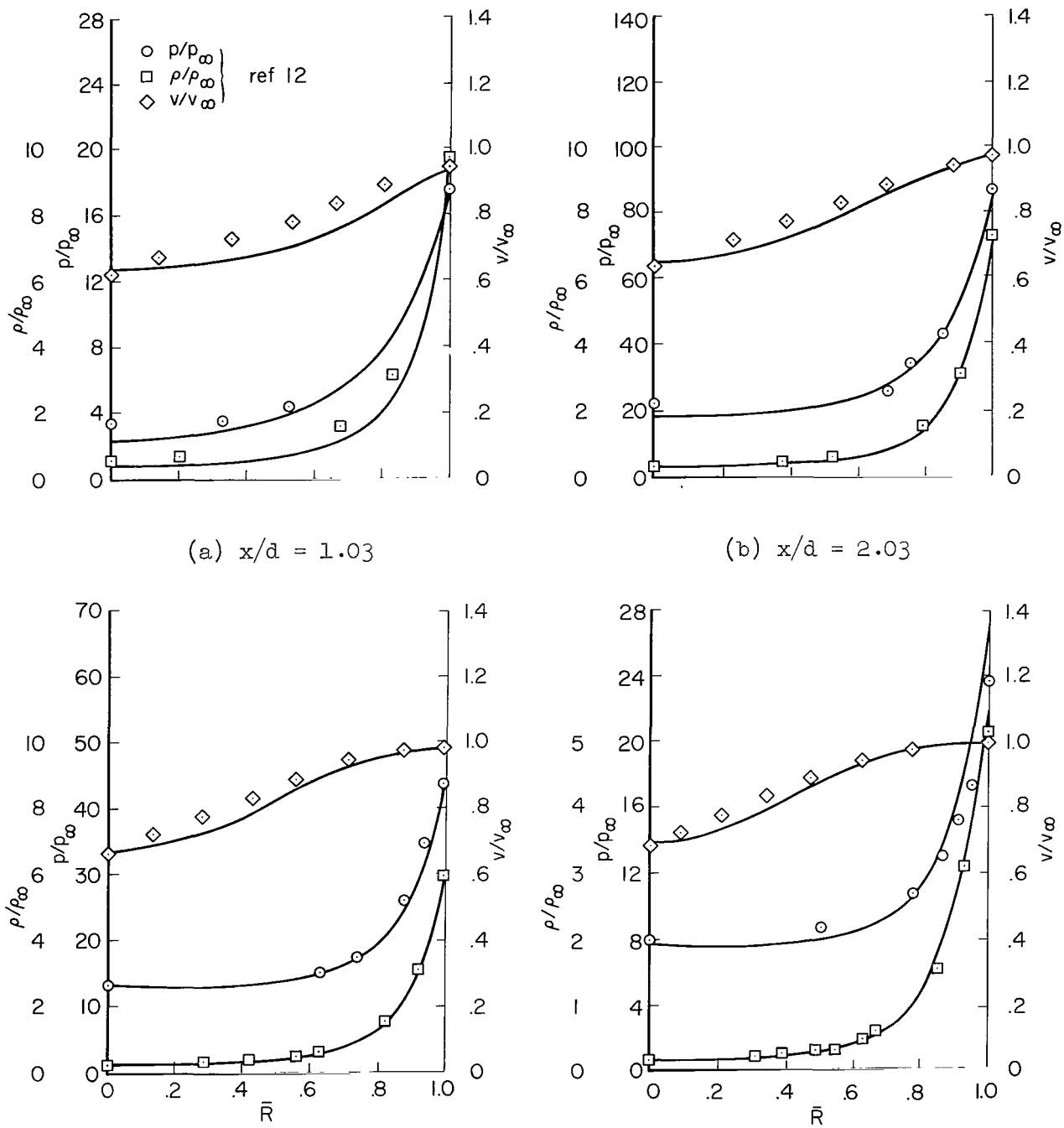

Figure 9.- Comparison of calculated flow fields over a hemisphere-cylinder at $M_\infty = 35.9$.

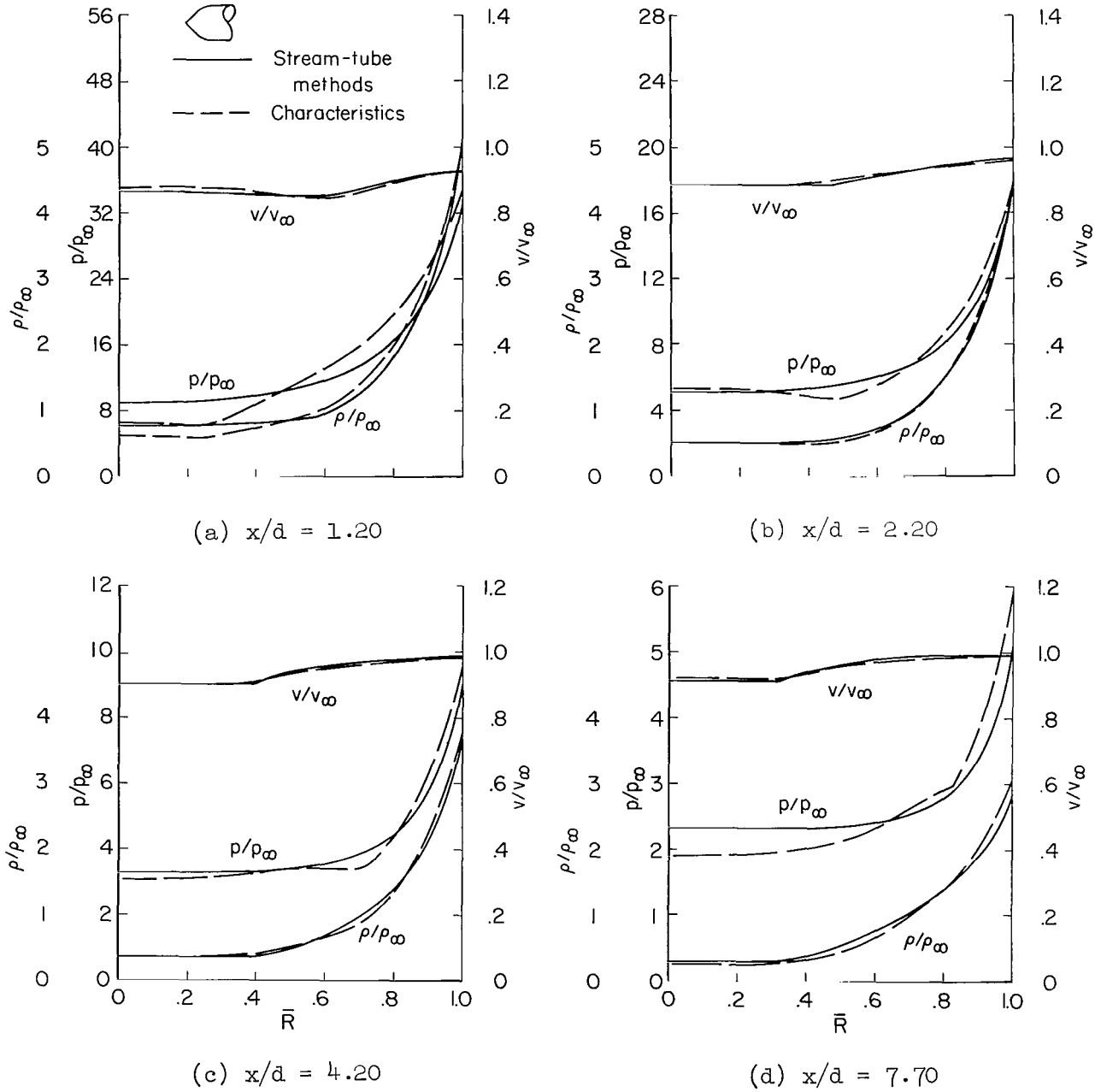

Figure 10.- Comparison of calculated flow fields over a 46° cone-sphere-cylinder at $M_\infty = 14.4$.

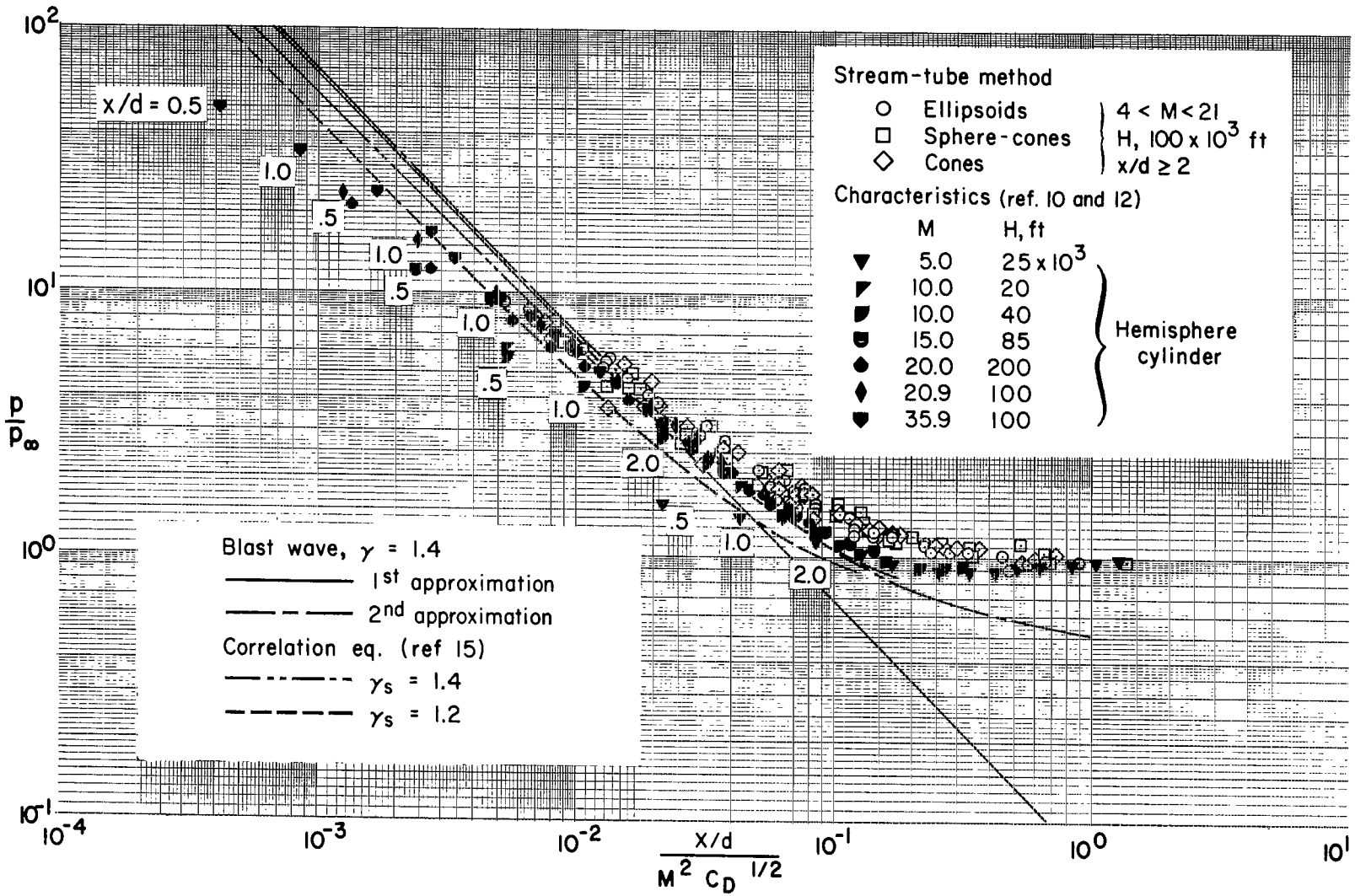

Figure 11.- Surface pressures on stream-alined cylinders.

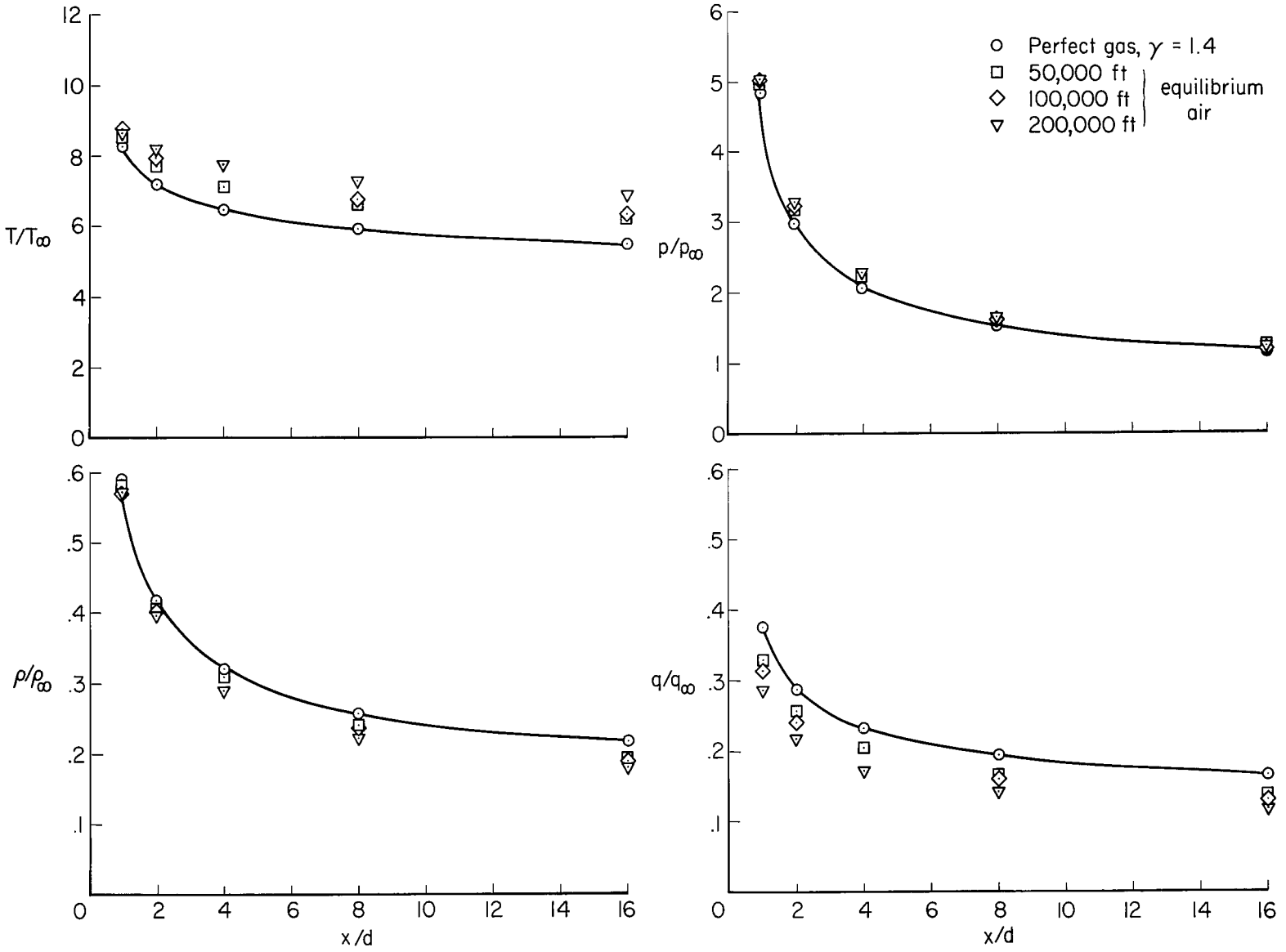

(a) M_∞ = 10.0

Figure 12.- Variation of flow properties over a hemisphere-cylinder.

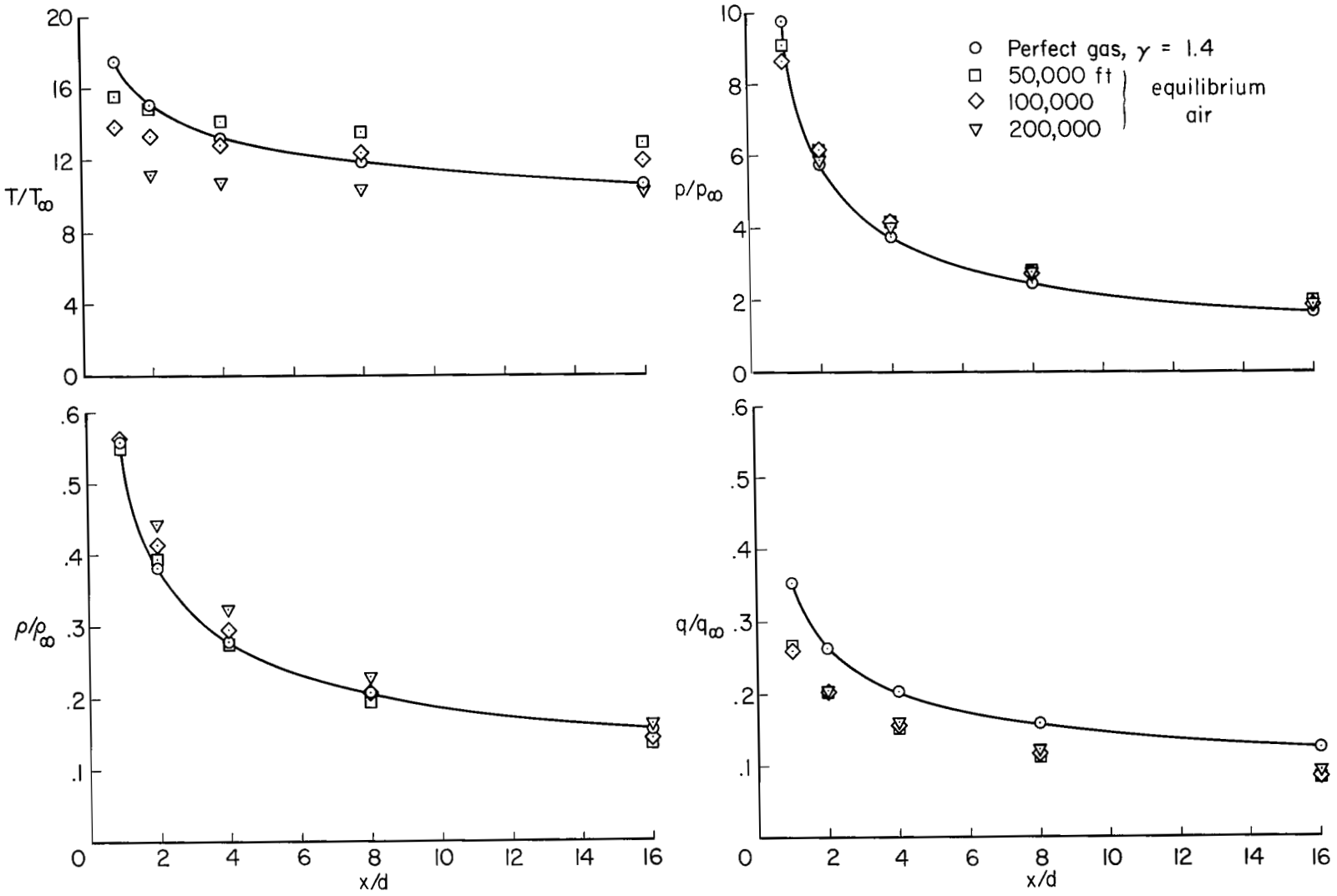

(b) $M_\infty = 15.0$

Figure 12.- Concluded.

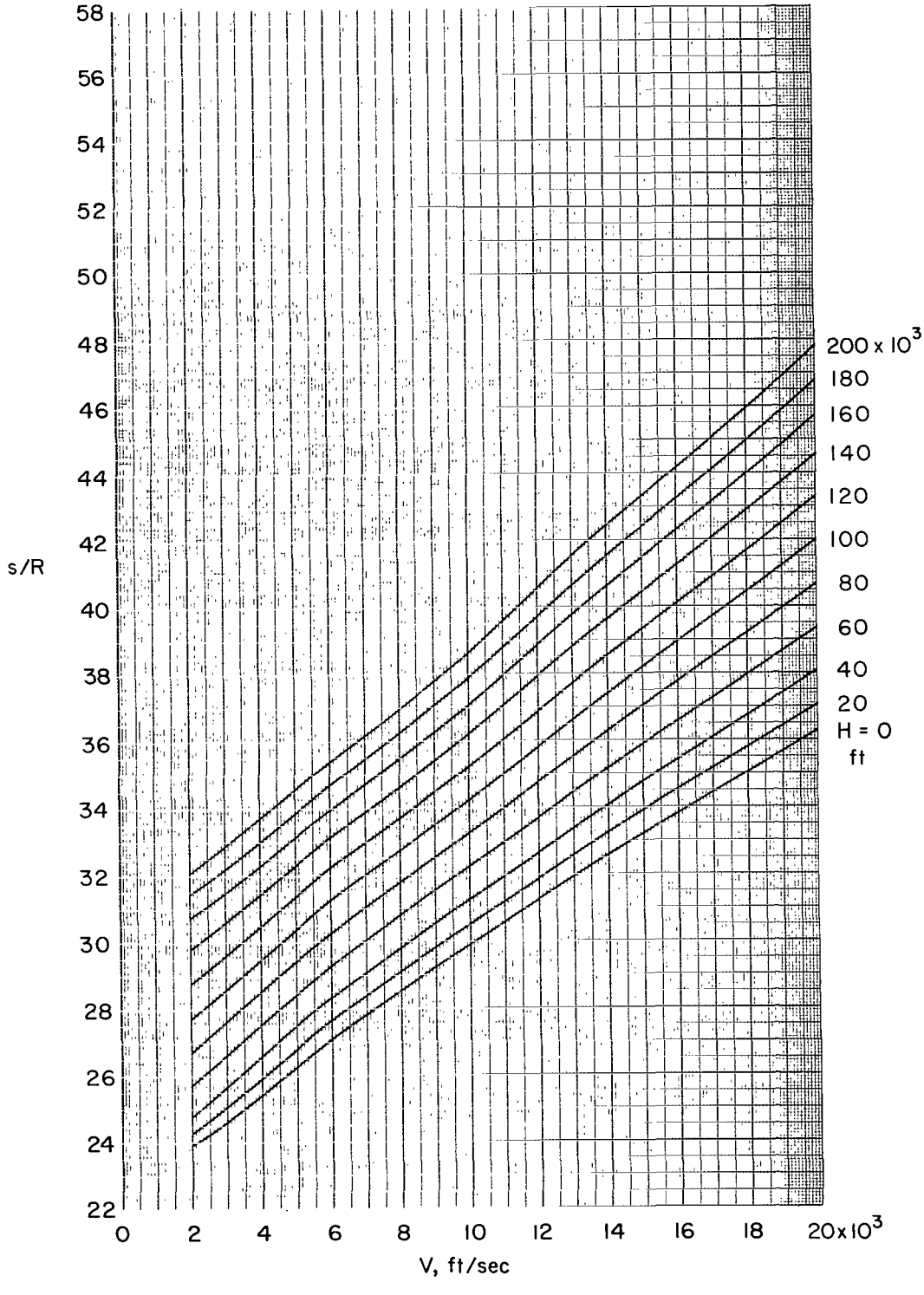

Figure 13.- Entropy behind a normal shock wave.

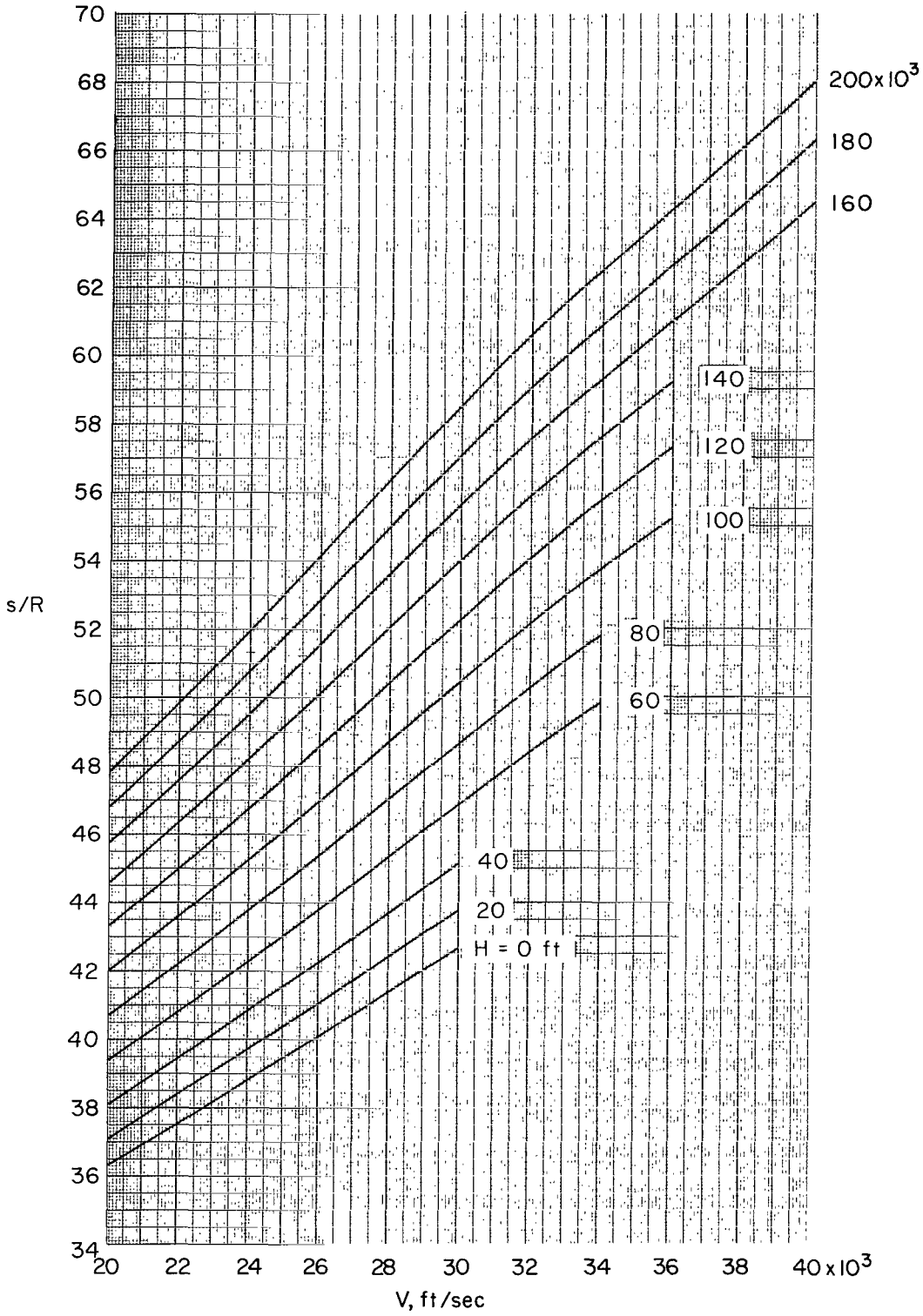

Figure 13.- Concluded.

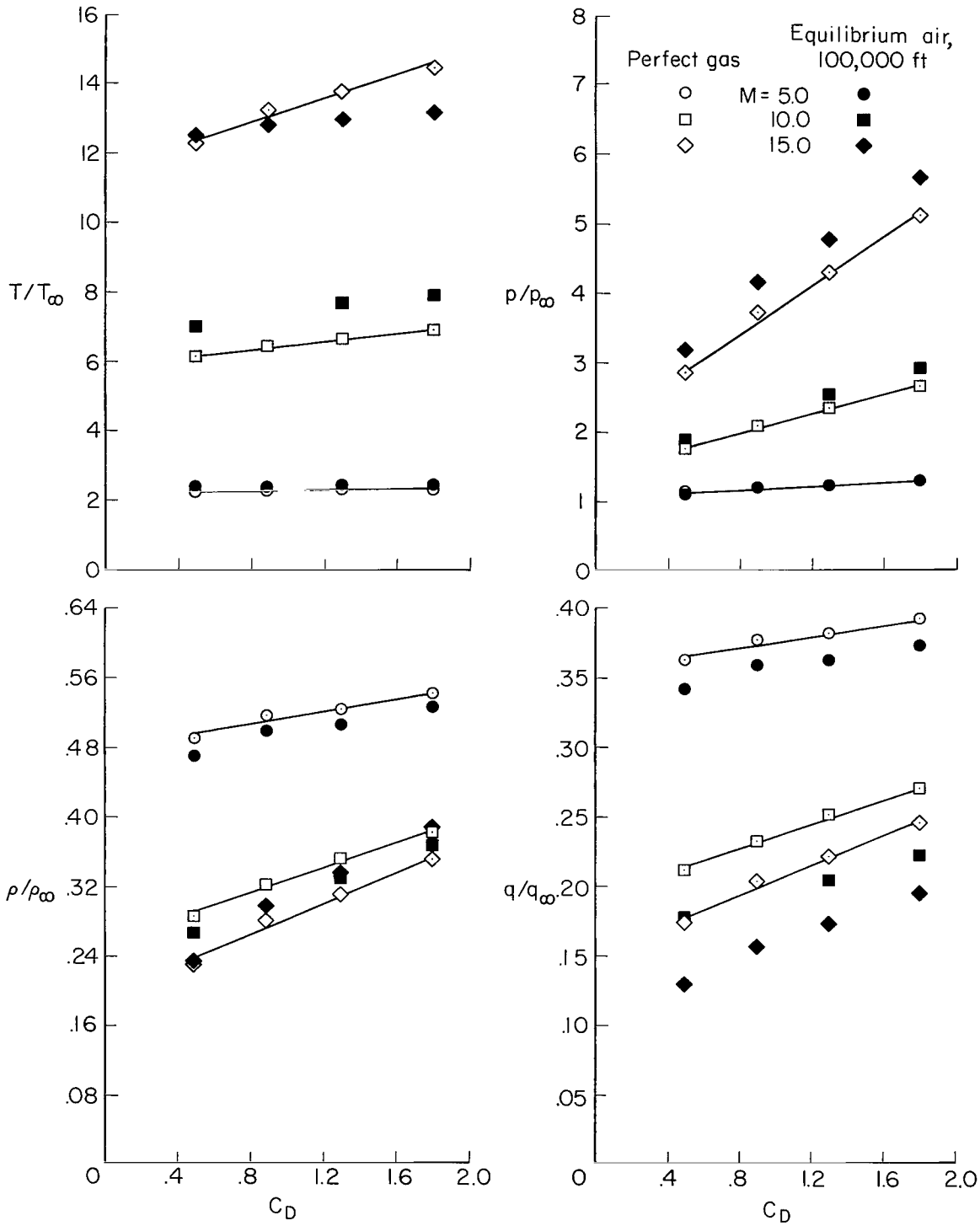

Figure 14.- Variation of flow properties with drag coefficient over ellipsoid-nosed-cylinders at $x/d = 4.0$.

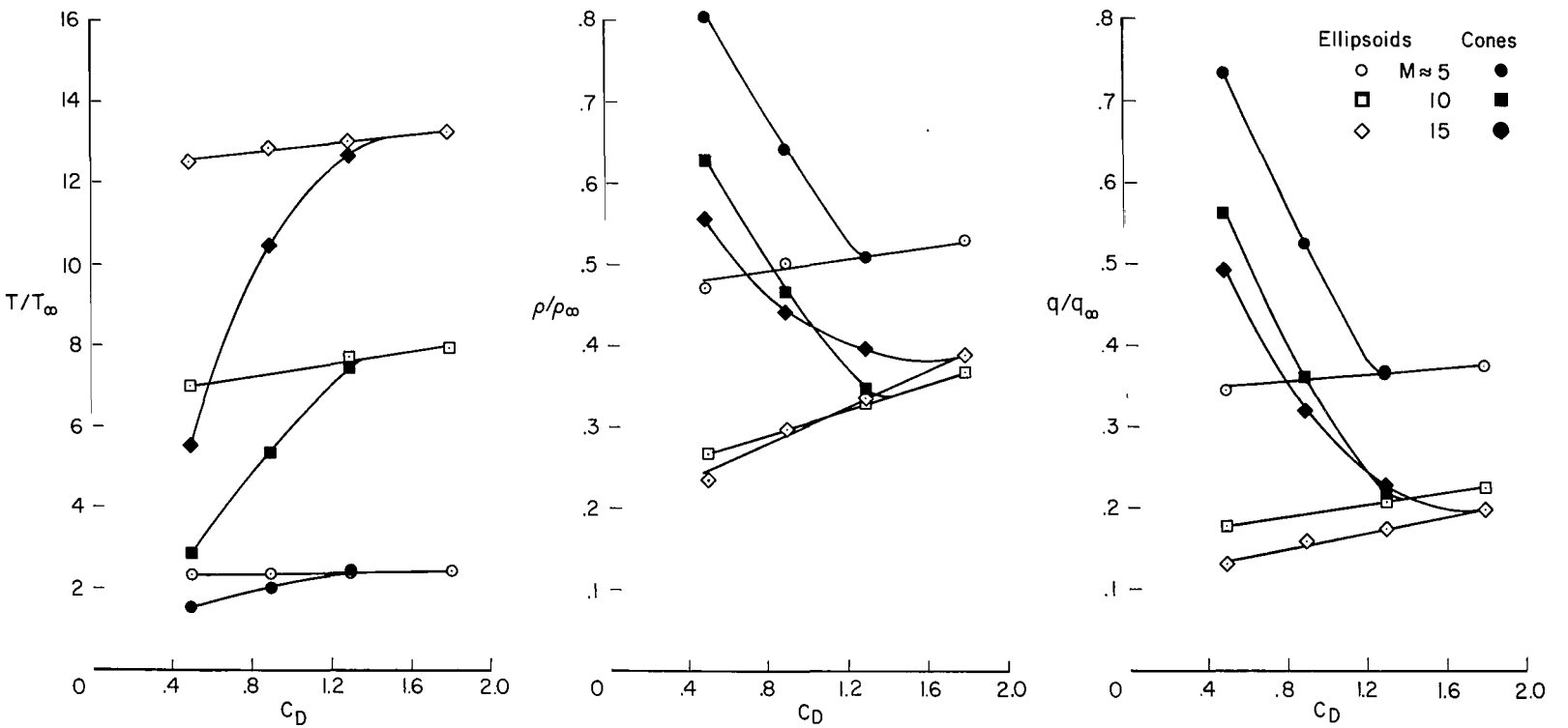

Figure 15.- Comparison between surface flow properties for cone-cylinders and ellipsoid-cylinders.

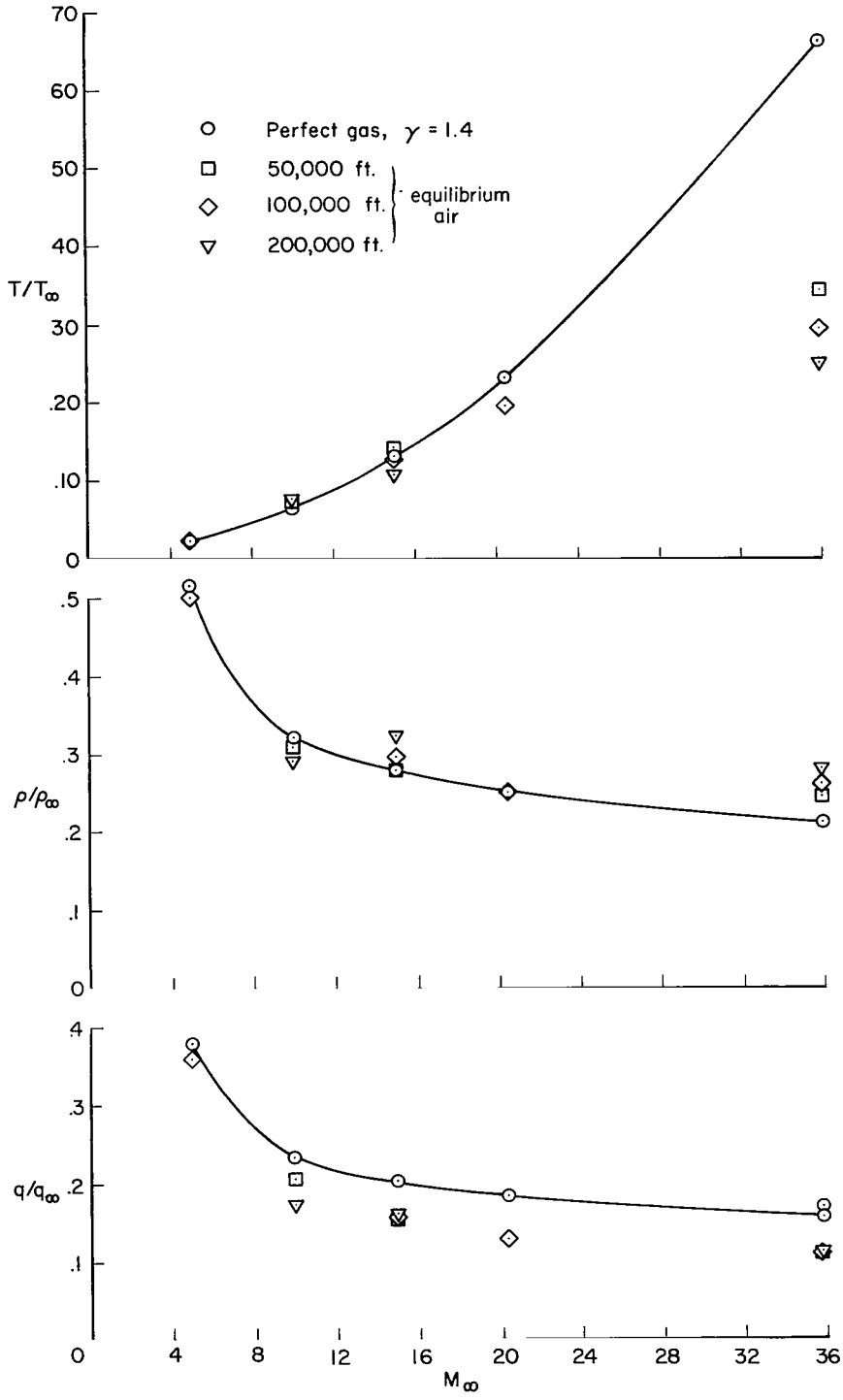

Figure 16.- Variation with Mach number of surface flow properties for a hemisphere-cylinder at x/d = 4.0.

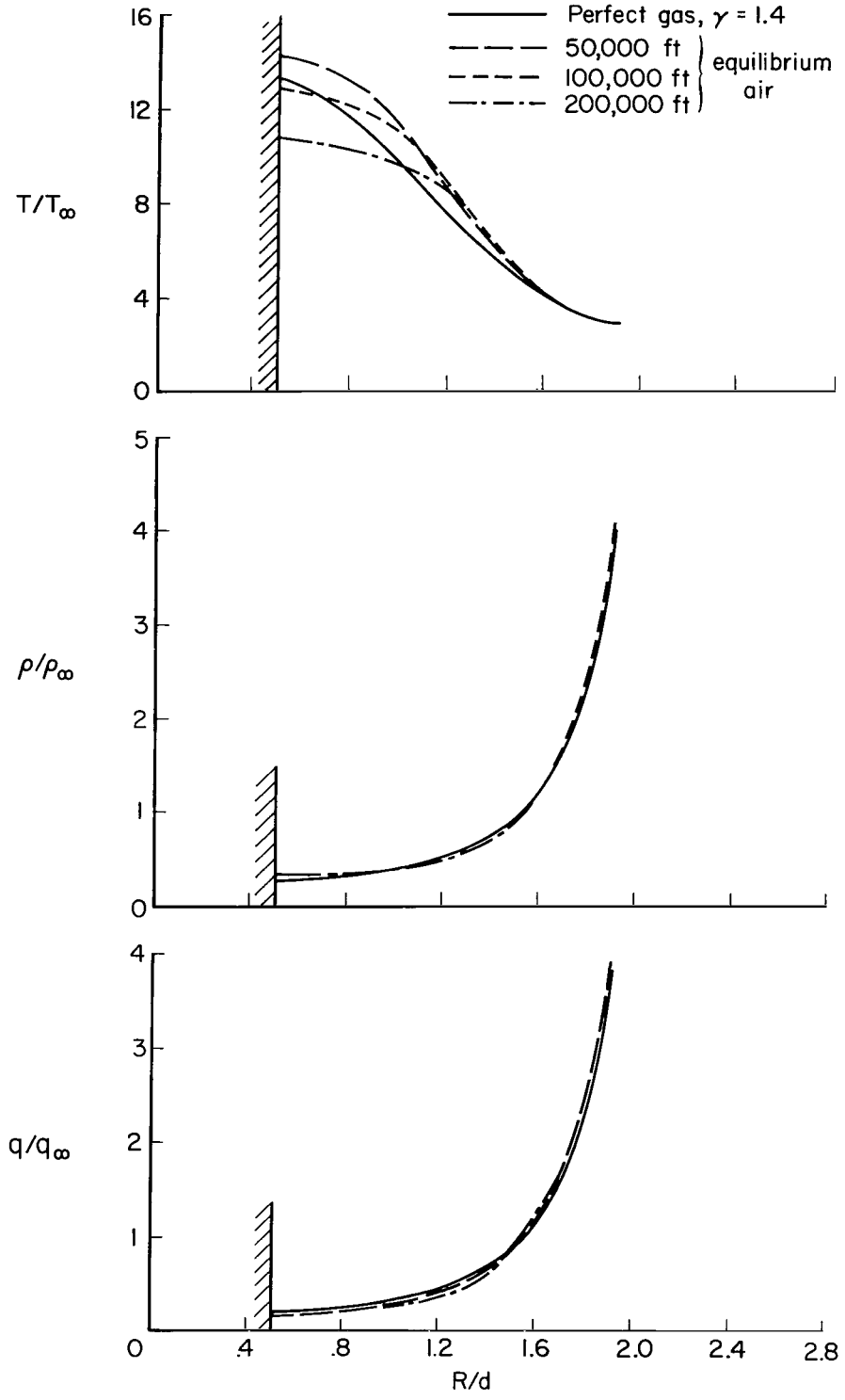

Figure 17.- Flow properties in shock layer over a hemisphere-cylinder at $x/d = 4.0$ at $M_\infty = 15.0$.

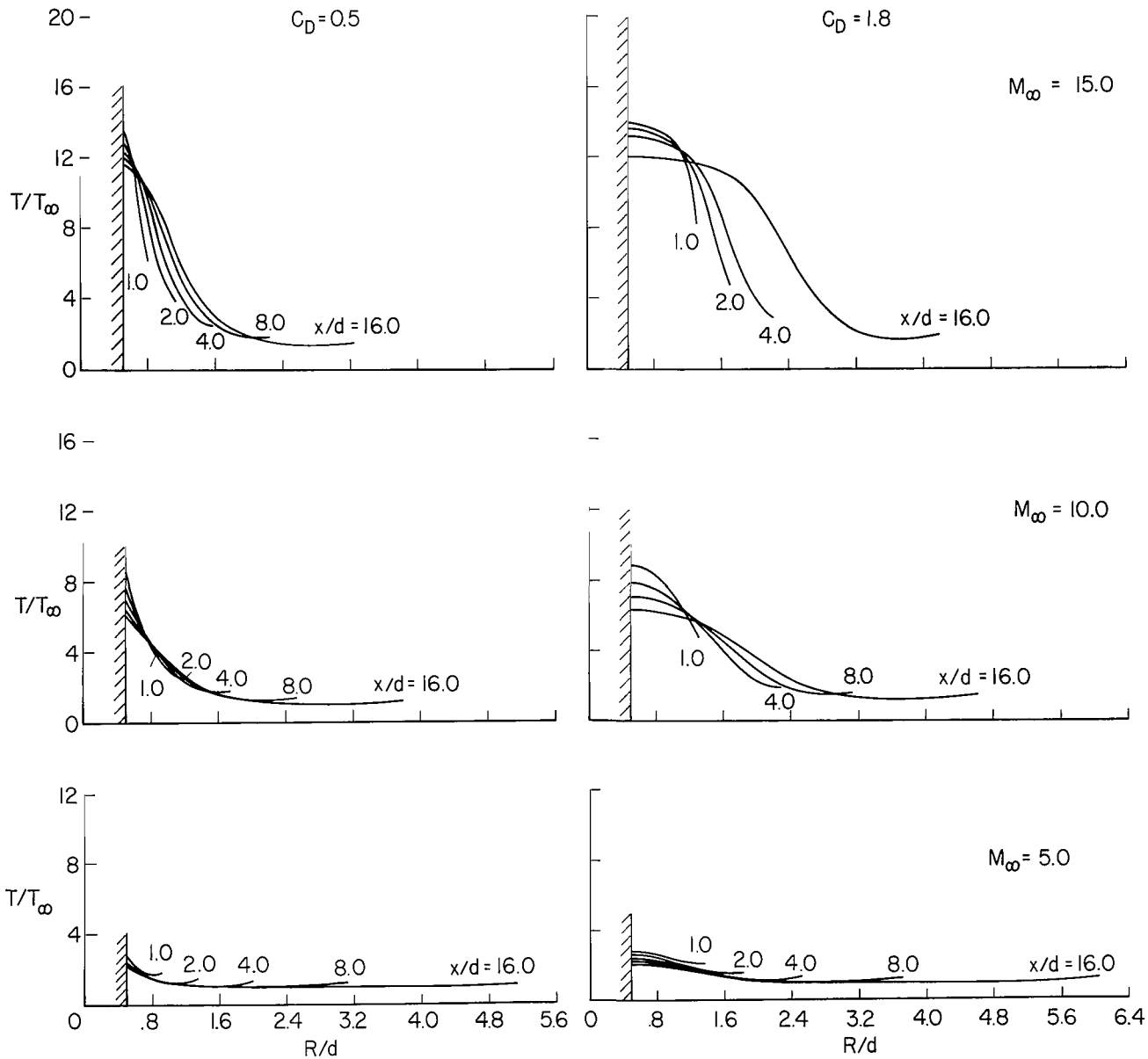

(a) Temperature ratio.

Figure 18.- Flow properties in shock layer over ellipsoid-nosed-cylinders.

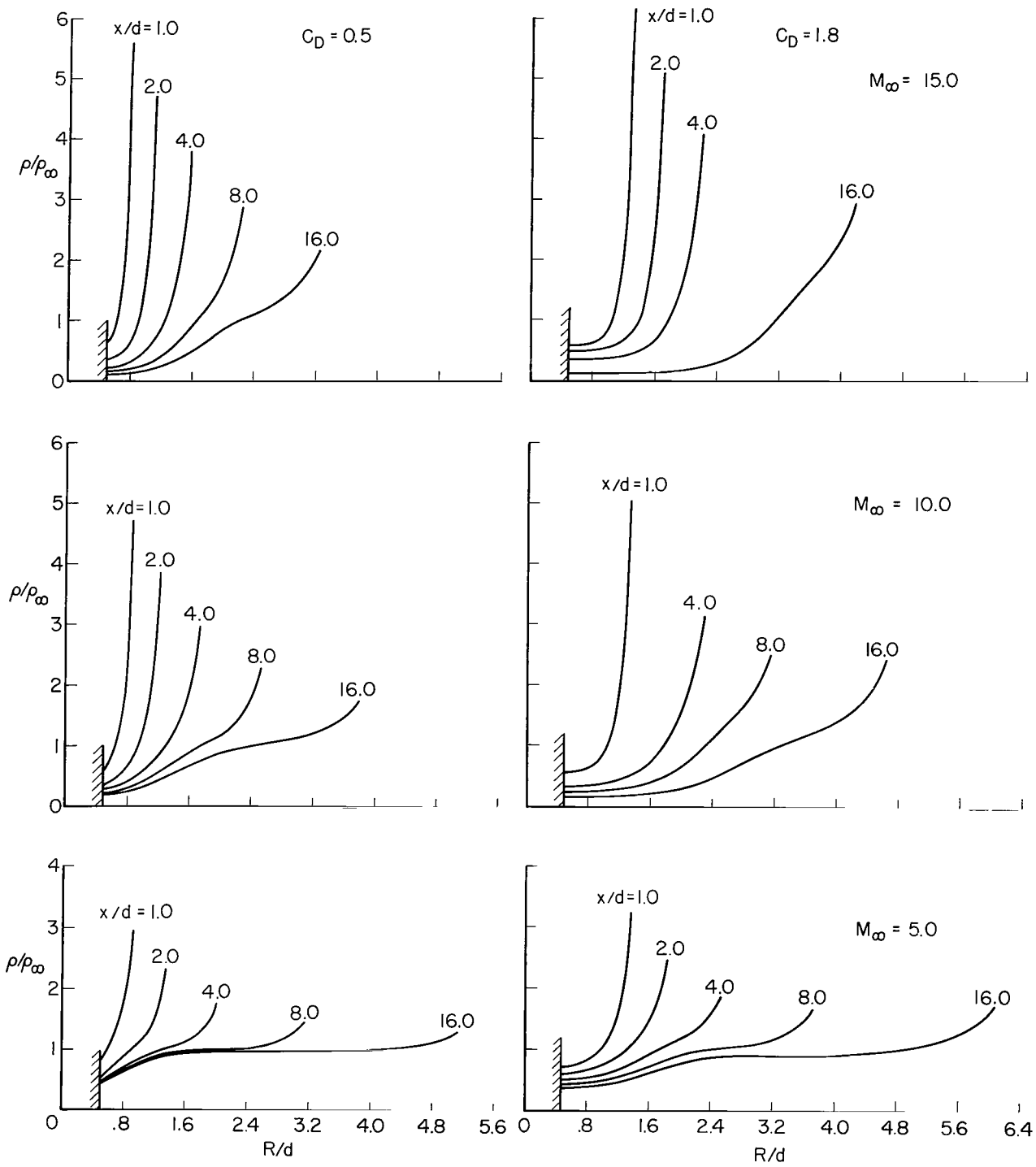

(b) Density ratio.

Figure 18.- Continued.

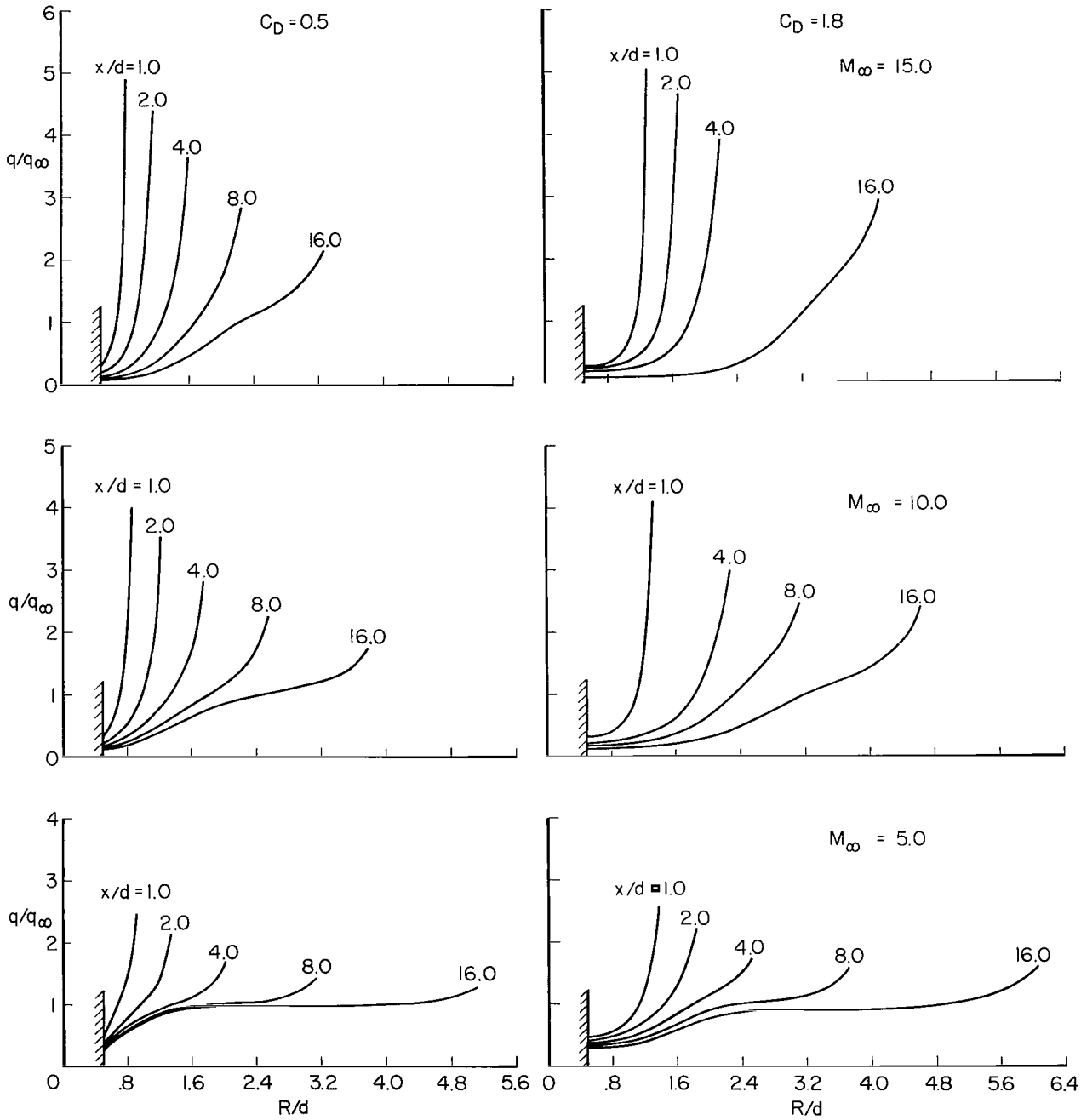

(c) Dynamic pressure ratio.

Figure 18.- Concluded.

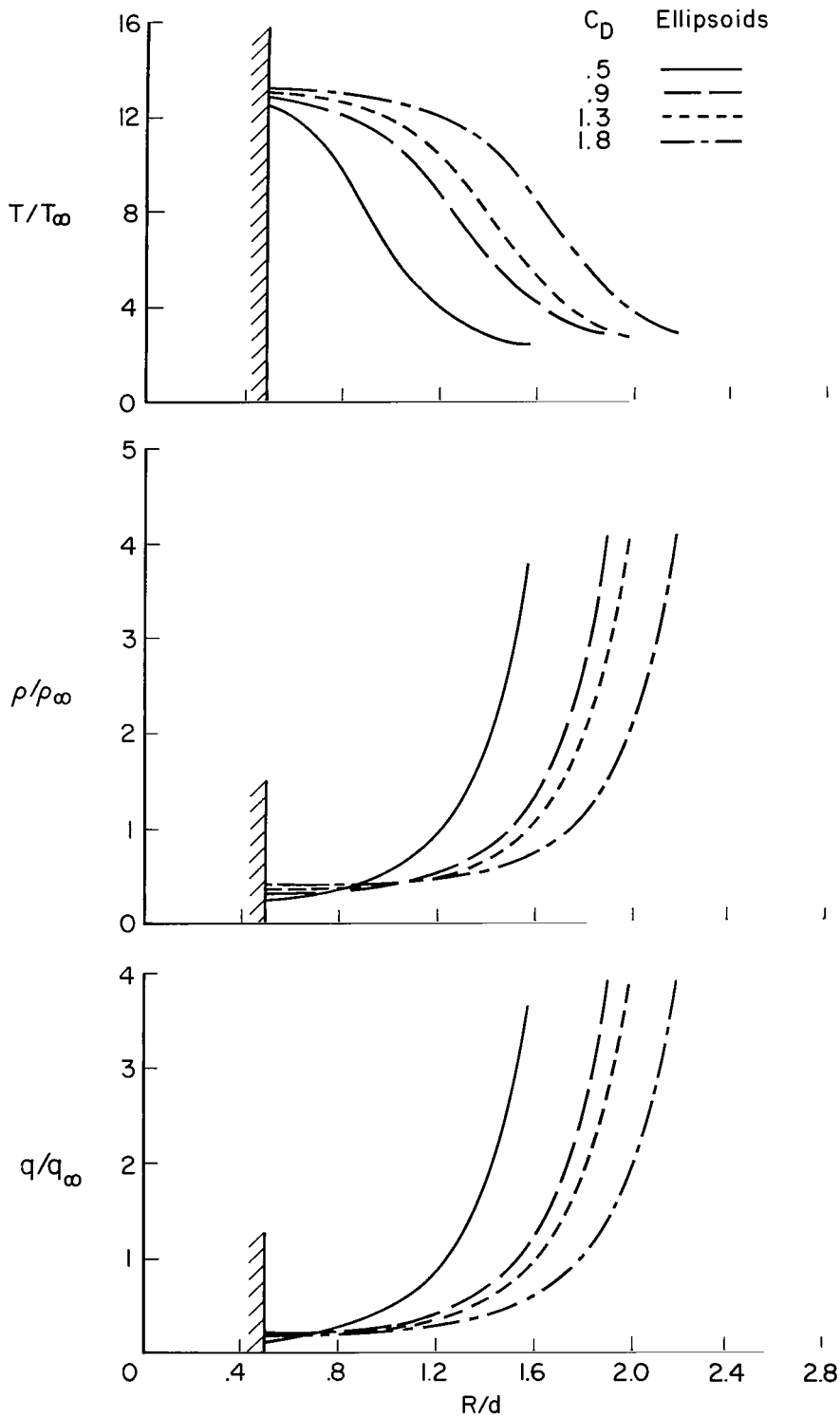

Figure 19.- Influence of drag coefficient on flow properties in shock layer of ellipsoid-nosed-cylinders at $x/d = 4.0$ at $M_\infty = 15.0$.

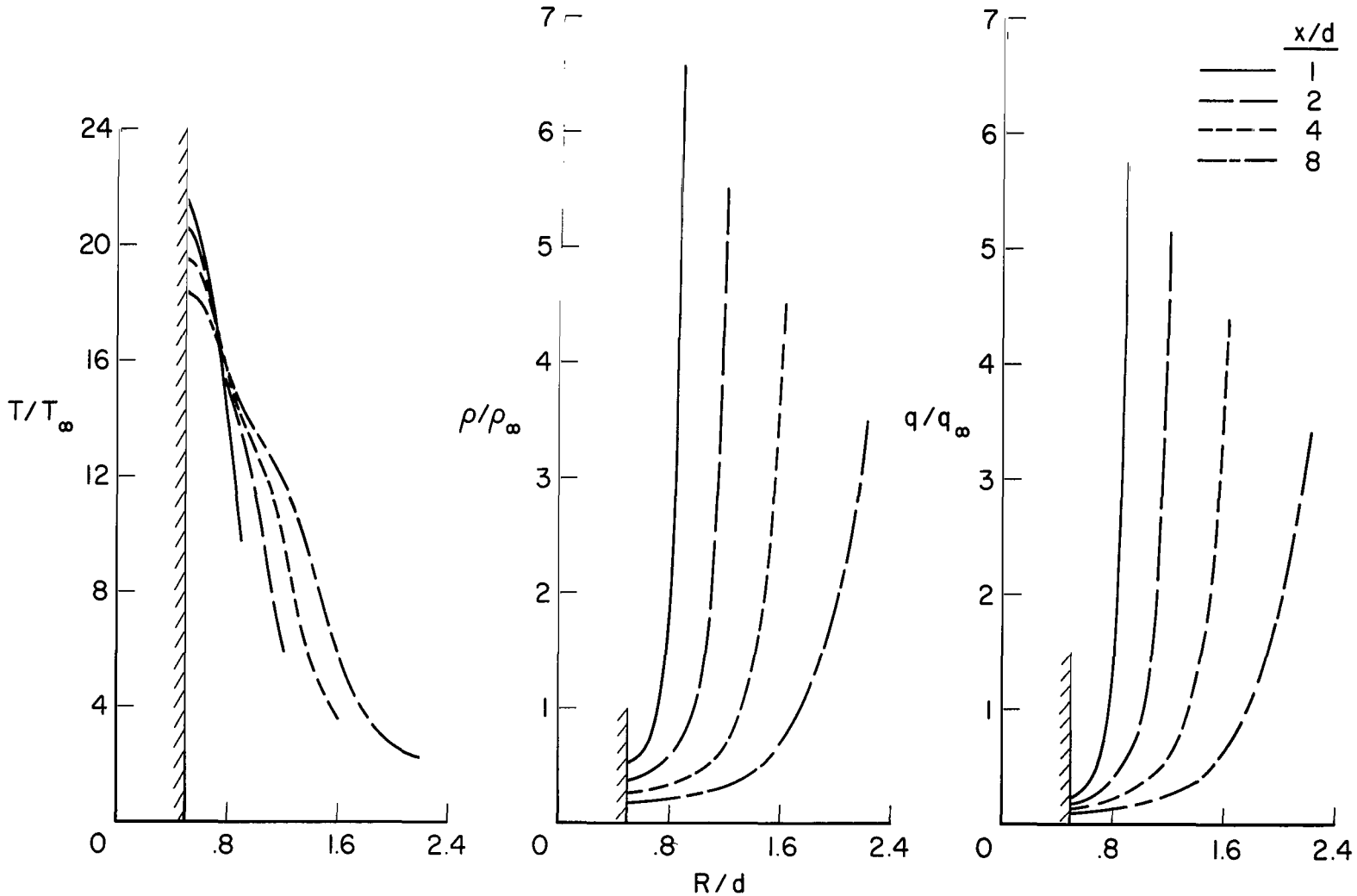

Figure 20.- Flow properties in shock layer over a hemisphere-cylinder at $M_\infty = 20.4$.

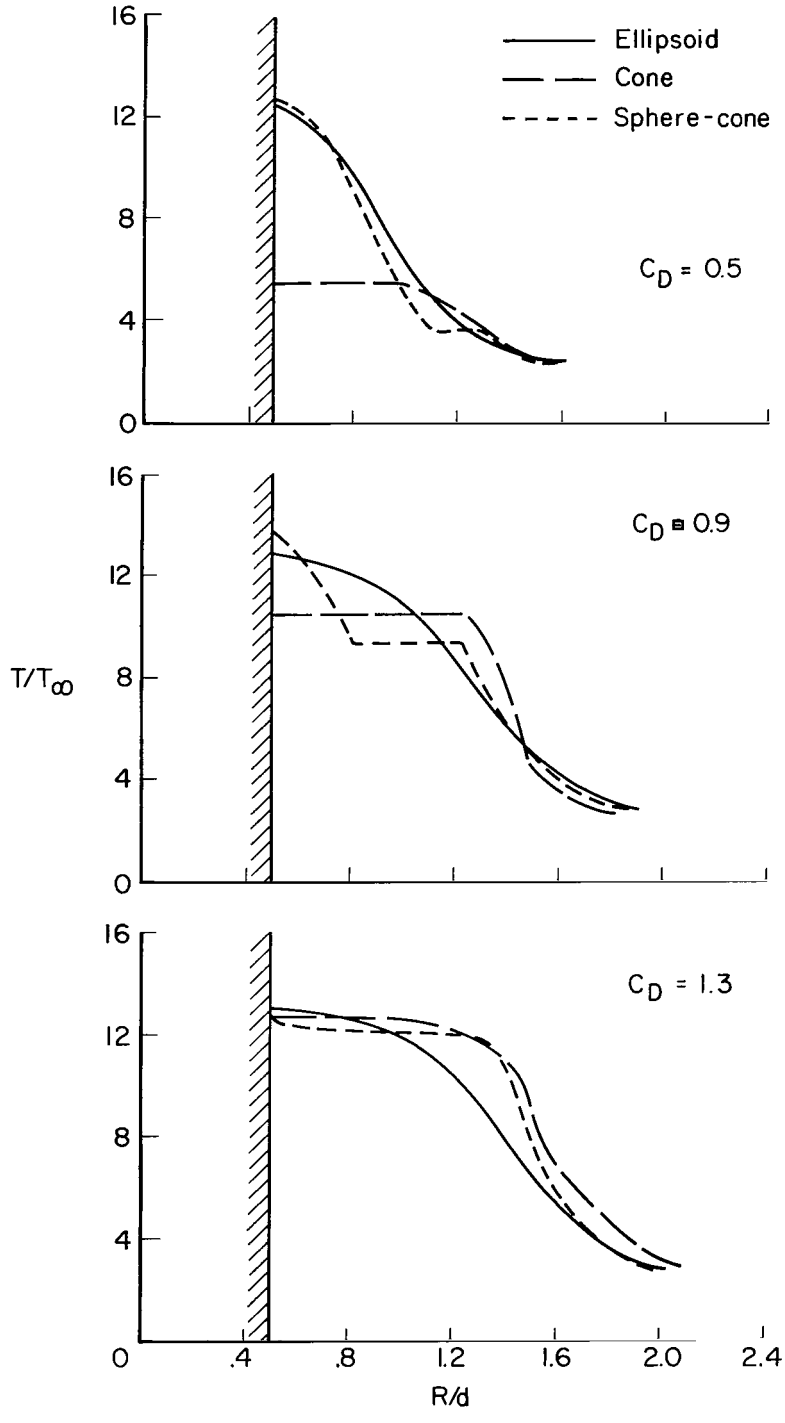

(a) Temperature ratio.

Figure 21.- Influence of nose shape on flow properties over cylinders at $M_\infty \approx 15$ at $x/d = 4.0$.

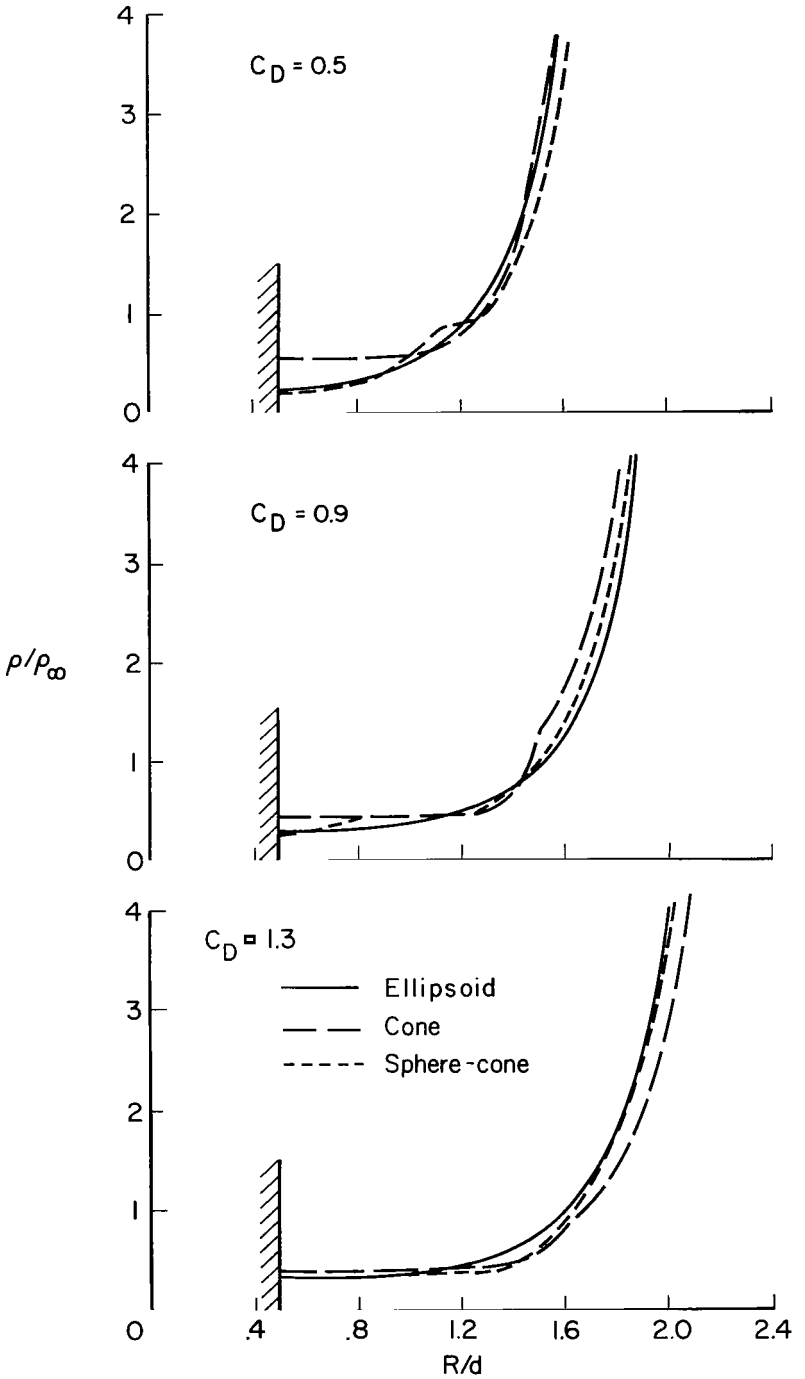

(b) Density ratio.

Figure 21.- Continued.

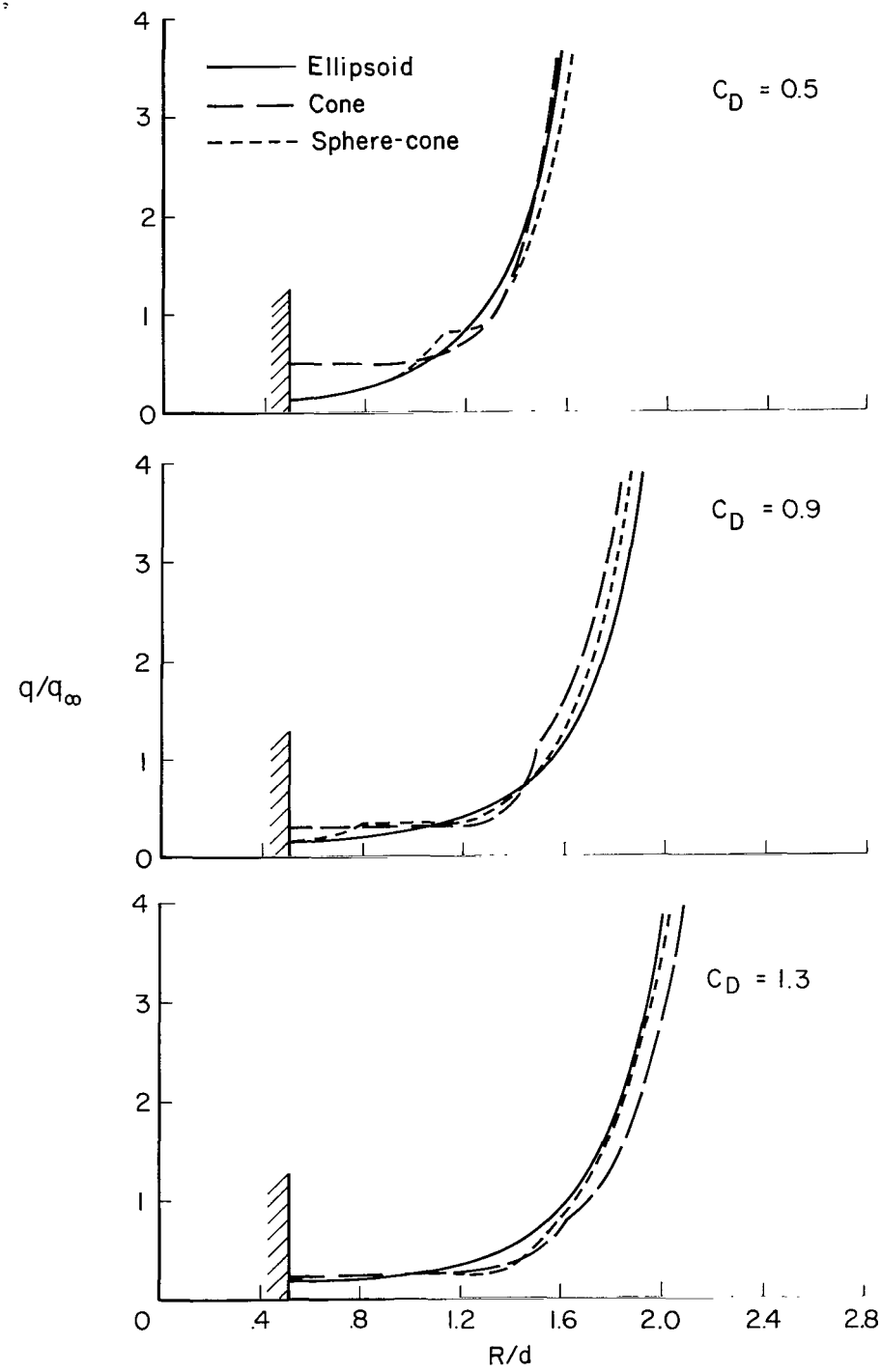

(c) Dynamic pressure ratio.

Figure 21.- Concluded.

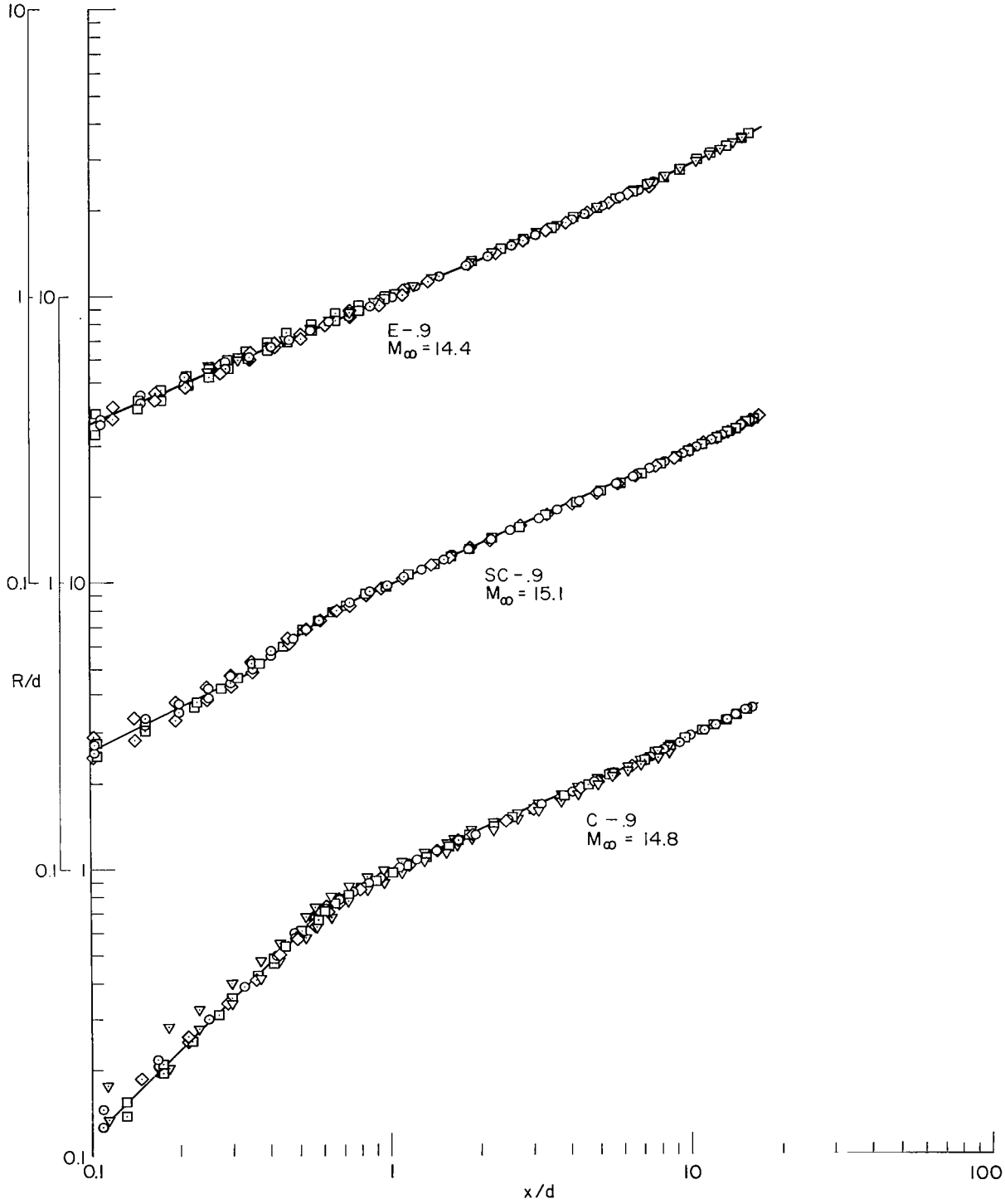

Figure 22.- Representative shock-wave profile measurements.

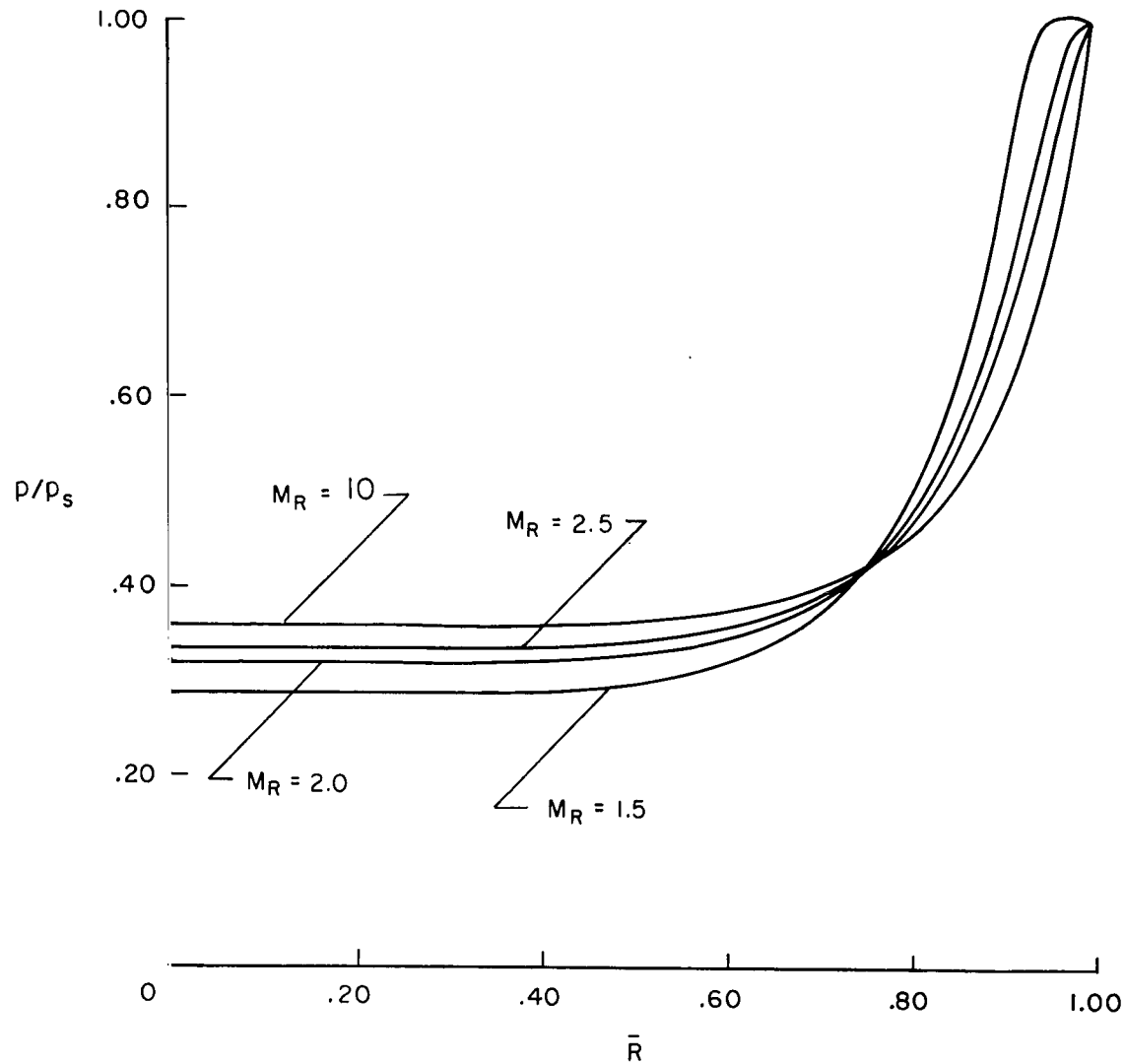

Figure 23.- Second approximation blast-wave prediction of radial pressure distribution for $\gamma = 1.4$.

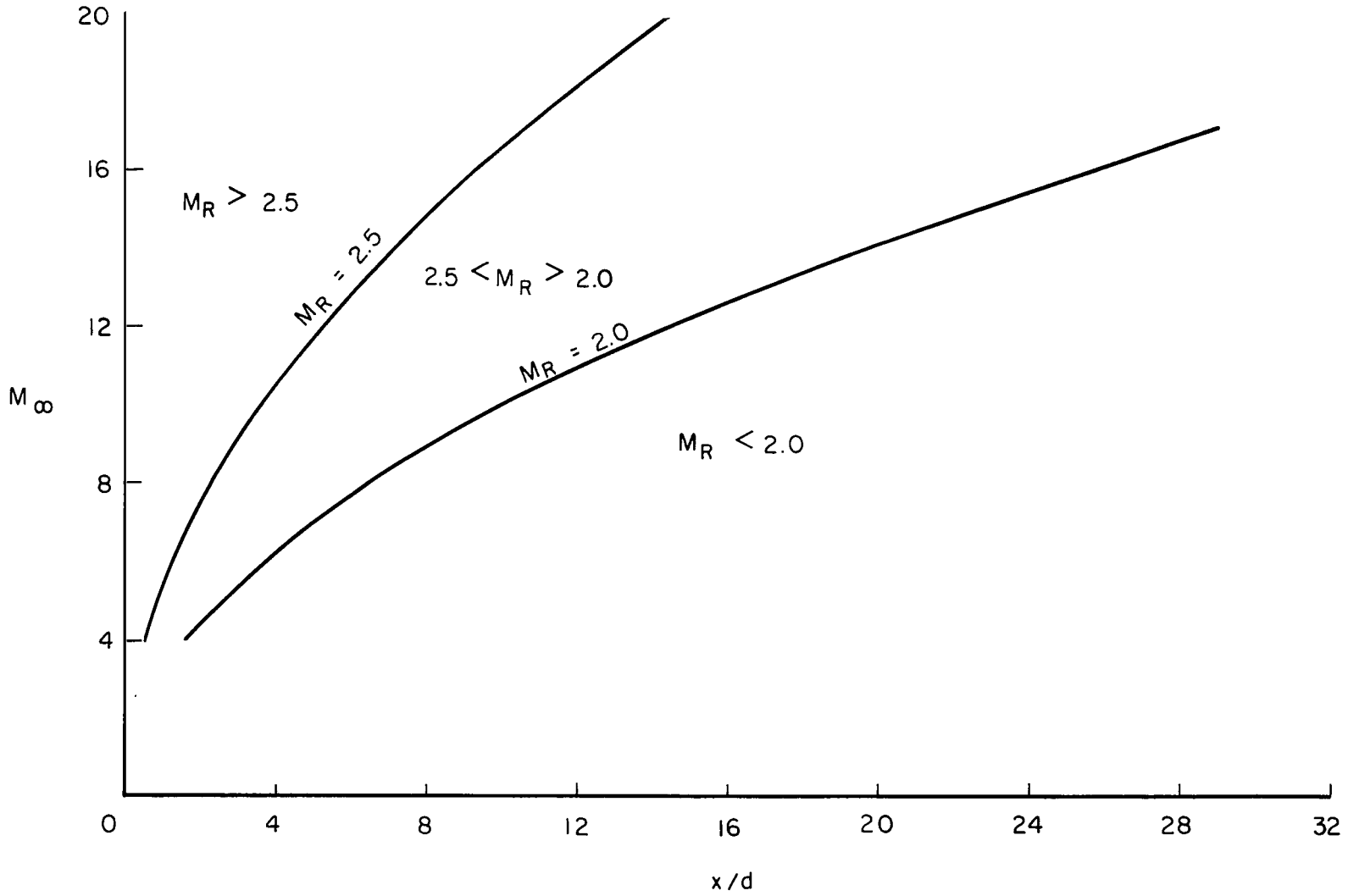

Figure 24.- Downstream limits of applicability of second approximation blast-wave theory for $C_D = 0.9$.